

Digging into the Interior of Hot Cores with ALMA (DIHCA). VII. Disk candidates around high-mass stars and evidence of anisotropic infall

FERNANDO A. OLGUIN ,^{1,2,3} PATRICIO SANHUEZA ,⁴ YOKO OYA ,¹ ADAM GINSBURG ,⁵ MARIA T. BELTRÁN ,⁶ KAHO MORII ,⁷ ROBERTO GALVÁN-MADRID ,⁸ HUEI-RU VIVIEN CHEN ,³ QIUYI LUO ,^{9,4} KEI E. I. TANAKA ,¹⁰ SUINAN ZHANG ,^{11,10,2} YU CHENG ,² FUMITAKA NAKAMURA ,^{2,12} SHANGHUO LI ,^{13,14} KOTOMI TANIGUCHI ,² GUIDO GARAY ,^{15,16} QIZHOU ZHANG ,⁷ MASAO SAITO ,^{2,17} TAKESHI SAKAI ,¹⁸ XING LU ,¹¹ JIXIANG WENG,¹¹ AND ANDRÉS E. GUZMÁN ,¹⁹

¹Center for Gravitational Physics, Yukawa Institute for Theoretical Physics, Kyoto University, Kitashirakawa Oiwakecho, Sakyo-ku, Kyoto 606-8502, Japan

²National Astronomical Observatory of Japan, National Institutes of Natural Sciences, 2-21-1 Osawa, Mitaka, Tokyo 181-8588, Japan

³Institute of Astronomy and Department of Physics, National Tsing Hua University, Hsinchu 30013, Taiwan

⁴Department of Astronomy, School of Science, The University of Tokyo, 7-3-1 Hongo, Bunkyo, Tokyo 113-0033, Japan

⁵Department of Astronomy, University of Florida, P.O. Box 112055, Gainesville, FL, USA

⁶INAF-Osservatorio Astrofisico di Arcetri, Largo E. Fermi 5, 50125 Firenze, Italy

⁷Center for Astrophysics | Harvard & Smithsonian, 60 Garden Street, Cambridge, MA 02138, USA

⁸Instituto de Radioastronomía y Astrofísica, Universidad Nacional Autónoma de México, Antigua Carretera a Pátzcuaro 8701, Ex-Hda. San José de la Huerta, Morelia, Michoacán, México C.P. 58089

⁹Institute of Astronomy, Graduate School of Science, The University of Tokyo, 2-21-1 Osawa, Mitaka, Tokyo 181-0015, Japan

¹⁰Department of Earth and Planetary Sciences, Institute of Science Tokyo, Meguro, Tokyo, 152-8551, Japan

¹¹Shanghai Astronomical Observatory, Chinese Academy of Sciences, 80 Nandan Road, Shanghai 200030, People's Republic of China

¹²Astronomical Science Program, The Graduate University for Advanced Studies, SOKENDAI, 2-21-1 Osawa, Mitaka, Tokyo 181-8588, Japan

¹³School of Astronomy and Space Science, Nanjing University, Nanjing, China

¹⁴Key Laboratory of Modern Astronomy and Astrophysics, Nanjing University, Ministry of Education, Nanjing, China

¹⁵Departamento de Astronomía, Universidad de Chile, Casilla 36-D, Santiago, Chile

¹⁶Chinese Academy of Sciences South America Center for Astronomy, National Astronomical Observatories, Chinese Academy of Sciences, Beijing, 100101, People's Republic of China

¹⁷Astronomical Science Program, The Graduate University for Advanced Studies, SOKENDAI, 2-21-1 Osawa, Mitaka, Tokyo 181-8588, Japan.

¹⁸Graduate School of Informatics and Engineering, The University of Electro-Communications, Chofu, Tokyo 182-8585, Japan.

¹⁹Joint Alma Observatory (JAO), Alonso de Córdova 3107, Vitacura, Santiago, Chile.

ABSTRACT

We study the kinematics of condensations in 30 fields forming high-mass stars with ALMA at a high-resolution of $\sim 0''.08$ on average (~ 230 au). The presence of disks is important for feeding high-mass stars without feedback halting growth as their masses increase. In the search for velocity gradients resembling rotation that can reveal the presence of disks, we analyze the emission of gas tracers in 49 objects using CH₃OH, CH₃CN, and tentative detections of HNCO and cis-HCOOH. Most of the velocity distributions show velocity gradients indicative of rotation. We reveal a total of 32 disk candidates, the largest sample to date that has been uniformly analyzed at a few hundred au scales in the high-mass regime. Their position-velocity maps are generally asymmetric with one side brighter than the opposite. We successfully fit a power law to the position-velocity maps of the disk candidates and find indices between -0.5 (Keplerian rotation) and -1 (rotation under specific angular momentum conservation) with a median of -0.7 . Under Keplerian rotation assumption, we estimate central masses, uncorrected for inclination, ranging between 7 to $45 M_{\odot}$. Excluding outliers, the disk candidates are relatively more compact (<200 au) and less massive ($<5 M_{\odot}$) than previous results at coarser angular resolution. We calculate an average Toomre- Q parameter and find that most are gravitationally unstable (median of 0.5). We conclude that these observations offer the first opportunity to separate the disk and envelope

components of hot cores on a statistically significant sample, and confirm that anisotropic collapse plays a role in feeding high-mass (proto)stars.

Keywords: Star formation (1569); Star forming regions (1565); Massive stars (732)

1. INTRODUCTION

The current paradigm of high-mass star formation requires non-spherical accretion of gas (e.g., H. W. Yorke & P. Bodenheimer 1999; M. R. Krumholz et al. 2009; A. J. Cunningham et al. 2011). This accretion flow can take the form of a disk: a flattened structure formed as a result of the conservation of angular momentum. Early search for these structures at (sub)mm wavelengths resulted in relatively large disks and/or toroidal structures with radii of the order of 1000 au (see M. T. Beltrán & W. J. de Wit 2016, and references therein). In addition to large sizes, these structures are massive, making them unstable and thus susceptible to fragmentation (allowing the formation of companions) or to develop substructures (e.g., spiral arms, K. G. Johnston et al. 2020). While these observations have been supported by simulations (e.g., R. Kuiper & T. Hosokawa 2018; B. Commerçon et al. 2022; D. M. A. Meyer et al. 2017), a newer picture has started to emerge with the raising number of high-resolution observations.

As the number of antennas of the Atacama Large Millimeter/submillimeter Array (ALMA) increased, the resulting higher sensitivity have allowed us to peek into scales smaller than 1000 au in a timely manner. These observations have allowed to find that disks in Galactic high-mass star-forming regions traced by dust emission can be more compact (radius < 500 au; e.g., J. D. Ille et al. 2018; L. T. Maud et al. 2019; C. Goddi et al. 2020; K. E. I. Tanaka et al. 2020; A. E. Guzmán et al. 2020; M. Fernández-López et al. 2023). Confirming that such structures indeed correspond to rotationally supported or Keplerian disks has only been done in a few cases compared to those detected in low-mass sources. An early search for disks around O-type star candidates by R. Cesaroni et al. (2017) only confirmed one Keplerian disk from kinematics, reveal rotation signatures around another two, and provided three additional tentative candidates. Case studies, as the one of L. T. Maud et al. (2019) in G17.64+0.16, have provided additional examples of Keplerian disks around O-type stars. C. Goddi et al. (2020) summarize disks-like structures observed by ALMA toward 14 hot cores forming O- and B-type stars and whose kinematics can be described by Keplerian rotation (their Appendix E). Most recent results have expanded in some of these regions. For instance, Y. Zhang et al. (2022) found individual disks surrounded

by a larger disk for the binary source G35.20-0.74 N core B initially studied by Á. Sánchez-Monge et al. (2013). Newer observations have also allowed detailed modeling of the kinematics with multiple molecular tracers to derive the disk properties (e.g., G339.88-1.23; Y. Zhang et al. 2019). Inside disk scales, tracers like water and salts have revealed Keplerian motions close to the forming stars (e.g., K. E. I. Tanaka et al. 2020; A. Ginsburg et al. 2023). In the northern hemisphere at latitudes only reachable by the IRAM/NOEMA interferometer, the CORE large program has provided 13 disk candidates from 800 au resolution observations (A. Ahmadi et al. 2023). Higher spatial resolution observations with IRAM/NOEMA targeting the Cygnus-X cloud found two Keplerian disks out of seven fragments (X. Pan et al. 2025, 300 au resolution). Nevertheless, a systematic search for rotating structures in high-mass star forming regions with ALMA at higher resolutions is lacking.

1.1. The DIHCA project

In order to study the kinematics of gas feeding high-mass (proto)stars we have observed 30 fields at high-angular resolution as part of the Digging into the Interior of Hot Cores with ALMA (DIHCA) project. These observations combine compact and extended ALMA 12m array configurations (see §2), and provide the continuum and line information necessary for detailed study of the gas distribution and kinematics of the inner 1000 au of hot cores. Case studies presenting the kinematics include G335.579-0.272 (F. A. Olgún et al. 2021, 2022, hereafter Paper I and II, respectively) and G336.01-0.82 (F. A. Olgún et al. 2023). Based on the compact configuration data, K. Taniguchi et al. (2023, hereafter Paper III) determined the systemic velocity and temperatures of the main cores, while K. Ishihara et al. (2024, hereafter Paper IV) cataloged the continuum cores. Using the same configuration, T. Sakai et al. (2025, hereafter Paper V) studied the deuterium fractionation of CH_3OH and determined the gas temperatures at peak $^{13}\text{CH}_3\text{OH}$ emission. The DIHCA sample selection is detailed in Paper IV, and it comprises bright nearby sources which have the potential to form high-mass stars as determined by previous studies. The sample list is presented in Table 1 and among its targets include the well studied fields G11.92-0.61

(C. J. Cyganowski et al. 2017; J. D. Ilee et al. 2018; C. J. Cyganowski et al. 2022; P. Sanhueza et al. 2025; S. Zhang et al. 2024), G29.96–0.02 (R. Cesaroni et al. 2017), G333.23–0.06 (S. Li et al. 2024), G333.46–0.16 (P. Saha et al. 2024), G335.579–0.272 (A. Avison et al. 2021, Paper I, Paper II), G343.12–0.06 (K. E. I. Tanaka et al. 2020; L. A. Zapata et al. 2024), G35.03+0.35 A (M. T. Beltrán et al. 2014), G35.20–0.74 N (Á. Sánchez-Monge et al. 2014; Y. Zhang et al. 2022), G351.77–0.54 (H. Beuther et al. 2019, 2025b; A. Ginsburg et al. 2023), G5.89–0.37 (L. A. Zapata et al. 2020; M. Fernández-López et al. 2021), IRAS 16562–3959 (A. E. Guzmán et al. 2020), IRAS 18089–1732 (H. Beuther et al. 2004; P. Sanhueza et al. 2021), IRAS 18162–2048 (GGD 27-MM1, N. Añez-López et al. 2020; M. Fernández-López et al. 2023; C. Carrasco-González et al. 2012), NGC 6334I (P. C. Cortés et al. 2024), NGC 6334I(N) (P. C. Cortés et al. 2021; S. Li et al. 2025), and W33A (L. T. Maud et al. 2017). Complementary to these studies, here we study the main condensations in these fields as well as secondary sources in them (if any). These condensations are over-dense structures where a single or a close multiple system is expected to form within cores. While cores can fragment into wider multiple systems, i.e., host one or more condensations, multiple systems in condensations are expected to form due to disk fragmentation. As such, we expect condensations to consist of at least one (proto)star with a gas envelope potentially hosting a circumstellar disk, hence the gas kinematics are increasingly dominated by the gravitational potential of the central source and rotation induced by the initial angular momentum of the core. In the DIHCA sample, low- to high-mass condensations in the cores identified in Paper IV are cataloged in Q. Luo et al. (2026, in press; hereafter Paper VI). This catalog uses PyBDSF²⁰ (N. Mohan & D. Rafferty 2015) to identify and fit 2-D Gaussians to the condensations from the continuum maps resulting in positions and radii, and exploits previous DIHCA efforts (Paper III) to assign temperatures to each condensation.

In this paper we present an overview of the kinematics at few hundred au resolution of the 30 observed fields in the DIHCA project with a focus on the rotation of gas structures. Except for a few individual cases, previous results lack the resolution to separate disk (a few hundred au in radius) and envelope (few hundred to thousands of au in radius) kinematics. This DIHCA study is designed to conduct the first systematic and statistical study on disk rotation in high-mass hot cores with suffi-

cient resolution. A detailed modeling of the kinematics with 2-D axisymmetric models will be the focus of a subsequent paper. The paper is structured as follows: §2 presents a summary of the observations and molecular gas tracers used, §3 presents the kinematics of the sources, §4 discusses our results, and §5 summarizes and presents our main conclusions.

2. OBSERVATIONS

The observations of the 30 fields were carried out by ALMA in band 6 (1.3 mm, 220 GHz; Project IDs: 2016.1.01036.S, 2017.1.00237.S; PI: Patricio Sanhueza) utilizing two array configurations. The compact configuration (C-5) observations were made during November 2016, May and July 2017, January and November 2018. The extended configuration (C-8) observations were performed during September and November 2017, and July 2019. A detailed description of the compact configuration data is presented in Paper IV, while Paper VI presents a summary of the extended configuration observations. We calibrated the data following the standard procedure with the appropriate CASA pipeline release (see Paper IV, Paper VI). Due to limitations on the data transfer on earlier observations, the channels of some spectral windows were averaged. Hence, some observations have a channel width of ~ 488.3 kHz ($\sim 0.63 - 0.67$ km s $^{-1}$), while others have channel widths equivalent to the spectral resolution (~ 976.5 kHz $\sim 1.26 - 1.34$ km s $^{-1}$).

With the exception of four fields (IRAS 18162–2048, NGC 6334I, NGC 6334I(N) and W33A), the continuum-subtracted visibilities were obtained using the procedure described in Paper I (GoCONTINUUM v2.0.0, F. Olgún & P. Sanhueza 2020). The phase centers of the visibilities for the extended and compact configurations were aligned (if needed) and then the visibilities were concatenated. For the remaining four fields, image artifacts were observed after imaging the continuum-subtracted visibilities in the form of negatives bowls in a specific direction common to all the bright continuum sources in some cases or curved spectra in others, probably introduced by the CASA task UVCONTSUB. To produce continuum-subtracted cubes for these four fields, we utilized STATCONT (Á. Sánchez-Monge et al. 2018) on the cubes produced by imaging the combined non continuum-subtracted visibilities with the corrected sigma-clip algorithm and a noise level of 1.5 mJy beam $^{-1}$. Although variations of the sigma-clip algorithm is used by both GoCONTINUUM (asymmetric sigma-clipping) and STATCONT, Paper I found that similar results are obtained. We use YCLEAN version v2.3.0 (F. Olgún 2025) to image CH₃OH $J_{K_a, K_e} = 18_{3,15} -$

²⁰ <https://pybdsf.readthedocs.io/en/latest/>

Table 1. CH₃OH $J_{K_a, K_c} = 18_{3,15} - 17_{4,14}$ A , $v_t = 0$ observations

Source	D (kpc)	Beam maj×min (P.A.)	Res. (au)	rms (mJy beam ⁻¹)	Chan. (kHz)
	(1)	(2)	(3)	(4)	(5)
G10.62–0.38	4.95	0''.075 × 0''.055 (76°)	320	1.2	976.452
G11.1–0.12	3.00	0''.074 × 0''.052 (74°)	190	1.2	976.452
G11.92–0.61	3.37	0''.074 × 0''.060 (88°)	220	1.2	976.452
G14.22–0.50 S	1.90	0''.072 × 0''.052 (68°)	120	1.5	488.285
G24.60+0.08	3.45	0''.112 × 0''.085 (−45°)	340	2.4	488.284
G29.96–0.02	5.26	0''.082 × 0''.072 (−80°)	400	1.7	488.295
G333.12–0.56	3.30	0''.111 × 0''.068 (−32°)	290	2.2	488.284
G333.23–0.06	5.20	0''.070 × 0''.041 (55°)	280	1.7	488.297
G333.46–0.16	2.90	0''.109 × 0''.068 (−32°)	250	2.0	488.284
G335.579–0.272	3.25	0''.070 × 0''.043 (50°)	180	1.8	488.298
G335.78+0.17	3.20	0''.109 × 0''.067 (−42°)	270	2.0	488.284
G336.01–0.82	3.10	0''.107 × 0''.069 (−43°)	270	2.2	488.285
G34.43+0.24 MM1	3.03	0''.078 × 0''.069 (77°)	220	1.6	488.294
G34.43+0.24 MM2	3.03	0''.128 × 0''.082 (−56°)	310	1.7	976.577
G343.12–0.06	2.90	0''.102 × 0''.072 (−79°)	250	1.4	488.292
G35.03+0.35 A	2.32	0''.078 × 0''.071 (82°)	170	1.6	488.294
G35.13–0.74	2.20	0''.126 × 0''.083 (−56°)	230	1.8	976.578
G35.20–0.74 N	2.19	0''.124 × 0''.107 (−73°)	250	1.7	488.294
G351.77–0.54	2.00	0''.139 × 0''.079 (−65°)	210	2.1	488.238
G5.89–0.37	2.99	0''.075 × 0''.055 (70°)	190	1.5	976.458
IRAS 16562–3959	2.39	0''.098 × 0''.069 (86°)	200	1.7	488.291
IRAS 18089–1732	2.34	0''.077 × 0''.055 (71°)	150	1.4	976.449
IRAS 18151–1208	3.00	0''.094 × 0''.054 (87°)	210	1.2	976.456
IRAS 18162–2048	1.30	0''.075 × 0''.060 (88°)	90	1.5	976.451
IRAS 18182–1433	3.58	0''.101 × 0''.054 (−87°)	260	1.4	976.457
IRAS 18337–0743	3.80	0''.108 × 0''.084 (−42°)	360	2.3	488.285
IRDC 18223–1243	3.40	0''.096 × 0''.055 (−88°)	250	1.3	976.455
NGC 6334I	1.35	0''.087 × 0''.065 (80°)	100	1.7	488.286
NGC 6334I(N)	1.35	0''.087 × 0''.067 (82°)	100	1.6	488.286
W33A	2.53	0''.074 × 0''.055 (78°)	160	1.2	976.449

NOTE—(1) Distance to the source. (2) Beam sizes correspond to the common beam within the selected range used for the moment maps. In general, the beam varies less than 1% within the selected ranges. (3) Spatial resolution derived from the geometric mean of the beam axes at the source distance. (4) Noise level estimated as the median absolute deviation of the data cube. (5) Channel width. A channel width of ~ 448.3 kHz corresponds to a velocity width of $\sim 0.63 - 0.67$ km s^{−1}. The spectral resolution is ~ 976.5 kHz.

$17_{4,14} A$, $v_t = 0$ (233.795666 GHz, $E_u/k_B = 447$ K) for the 30 fields (Table 1). The YCLEAN code automatically and iteratively produces incremental masks and cleaning thresholds based on the beam secondary lobe level (Y. Contreras et al. 2018) which are then used by the CASA TCLEAN task to produce clean cubes. For the TCLEAN task, we used the Hogbom deconvolver with Briggs weighting and a robust parameter of 0.5. In addition, for a subset of 22 fields we image an entire spectral window where the CH_3CN $J_K = 12_K - 11_K$ ladder is located (hereafter 220 GHz spectral window) using YCLEAN, which is the only spectral window with the two channels per spectral resolution element for all fields (Table 2). The chosen CH_3OH transition has shown good results not only tracing rotating structures but also substructures like accretion flows (e.g., F. A. Olgun et al. 2023), even considering that its E_u/k_B is relatively high. CH_3CN is a well known kinematics tracer, however it may trace more extended gas and could easily become optically thick toward the central sources (e.g., F. A. Olgun et al. 2022) and has slightly lower angular resolution in our observation setup (typically a 20 au difference in spatial resolution and up to 80 au in the worst case, cf. Tables 1 and 2). In particular cases, we use additional lines in an attempt to extract as much information about the kinematics as possible. Hence, when the CH_3OH transition is marginally or not detected or more channels per line are needed to explore the kinematics we use CH_3CN $J_K = 12_3 - 11_3$ (220.7090165 GHz, $E_u/k_B = 133$ K). When these two fail, we explore other lines in the 220 GHz spectral window (Table 3). See §4.4 for a discussion of the implications on the derived source properties when using different tracers.

2.1. Ancillary data

We use the DIHCA compact configuration data targeting the SiO $J = 5 - 4$ transition (217.10498 GHz) to search for outflows not reported in the literature. Although these data have lower angular resolution ($> 0''.5$), outflows are expected to be extended thus its emission can be better recovered by the compact configuration. These data are only used to determine the direction of potential outflows and support the rotation origin of any velocity gradient detected in the molecules above. A detailed study is necessary to confirm these outflows. Nevertheless, these data were reduced in the same way as those in Paper I using YCLEAN with TCLEAN’s multi-scale deconvolver (scales 0, 5, 15) and Briggs weighting with a robust parameter of 0.5.

3. RESULTS

We follow the condensation naming and positions from the source catalog presented in Paper VI. Here

we analyze the line emission from 49 condensations in CH_3OH $J_{K_a,K_c} = 18_{3,15} - 17_{4,14} A$, $v_t = 0$ (19 condensations), CH_3CN $J_K = 12_3 - 11_3$ (26 condensations), HNCO $J_{K_a,K_c} = 10_{0,10} - 9_{0,9}$ (1 condensation) and $J_{K_a,K_c} = 10_{3,8} - 9_{3,7}$ (2 condensations), and c-HCOOH $J_{K_a,K_c} = 10_{4,6} - 9_{4,5}$ (1 condensation). Hereafter, we will refer to sources and condensations indistinctly.

3.1. Line emission

Table 4 lists all the observed fields and their respective condensations (if any) where molecular line emission was detected over the 5σ level (with σ typically in the 1.0–2.5 mJy beam $^{-1}$ range). Of the 30 imaged fields, molecular line emission over the 5σ level from the aforementioned transitions was detected toward 25 fields. The total number of condensations with line emission in these 25 fields is 49. The fields not listed in Table 4 are: G24.60+0.08, G34.43+0.24 MM2, IRAS 18151–1208, IRAS 18337–0743, and IRDC 18223–1243. Of these, CH_3CN emission is marginally detected over the 5σ level in a few cores in IRAS 18151–1208, G24.60+0.08 and IRDC 18223–1243, but not extended enough to resolve their kinematics. Although line emission was detected toward some of these fields in the compact configuration data at core scales (e.g., IRDC 18223–1243; Paper III), the combined dataset does not provide enough valid pixels for a study of their kinematics. In G34.43+0.24 MM2 and IRAS 18337–0743 neither molecule is detected over the 5σ level toward the cataloged condensations, likely due to the low sensitivity of the observation setup combined with fainter line emission in these sources. Other sources in the fields listed in Table 4 that may be forming high-mass stars also do not show significant line emission to properly study their kinematics (e.g., G14.22–0.50 S ALMA2). Additional observations with higher sensitivity may help to study the kinematics in these sources in the future.

Figure 1 shows the first order moment maps (intensity weighted velocity) toward individual condensations. As expected from their upper-level energies E_u/k_B , the selected transition of CH_3OH is relatively more compact than the CH_3CN one, with the former generally tracing closer to the continuum emission. There are sources, however, where CH_3OH is more extended than the continuum at the 5σ level (e.g., G335.579–0.272 ALMAe1, G35.20–0.74 N ALMAe1). On the other hand, there are sources whose velocity gradient is not clear (e.g., NGC 6334I(N) ALMAe1) or first moment map emission is compact (e.g., IRAS 16562–3959 ALMAe5). These may be the result of line emission becoming optically thick toward the peak continuum intensity or absorbed by the continuum, or the sensitivity is insufficient. Nev-

Table 2. CH₃CN $J_K = 12_3 - 11_3$ observations

Source	Beam	Res.	rms	Chan.
		maj \times min (P.A.)		
G10.62–0.38	0. $''$ 081 \times 0. $''$ 065 (90 $^{\circ}$)	360	1.5	488.226
G11.1–0.12	0. $''$ 081 \times 0. $''$ 059 (79 $^{\circ}$)	210	1.2	488.226
G11.92–0.61	0. $''$ 101 \times 0. $''$ 076 (–68 $^{\circ}$)	300	1.2	488.225
G14.22–0.50 S	0. $''$ 076 \times 0. $''$ 054 (64 $^{\circ}$)	120	1.6	488.285
G24.60+0.08	0. $''$ 115 \times 0. $''$ 091 (–43 $^{\circ}$)	350	2.2	488.284
G333.12–0.56	0. $''$ 116 \times 0. $''$ 077 (–34 $^{\circ}$)	310	1.9	488.284
G333.23–0.06	0. $''$ 077 \times 0. $''$ 043 (55 $^{\circ}$)	300	1.6	488.297
G333.46–0.16	0. $''$ 114 \times 0. $''$ 076 (–33 $^{\circ}$)	270	2.0	488.284
G34.43+0.24 MM2	0. $''$ 120 \times 0. $''$ 079 (–57 $^{\circ}$)	300	1.8	488.288
G35.03+0.35 A	0. $''$ 085 \times 0. $''$ 077 (–88 $^{\circ}$)	190	1.9	488.294
G35.13–0.74	0. $''$ 119 \times 0. $''$ 079 (–57 $^{\circ}$)	210	1.9	488.289
G5.89–0.37	0. $''$ 088 \times 0. $''$ 077 (–34 $^{\circ}$)	250	1.7	488.229
IRAS 16562–3959	0. $''$ 108 \times 0. $''$ 065 (82 $^{\circ}$)	200	1.5	488.291
IRAS 18089–1732	0. $''$ 096 \times 0. $''$ 078 (–36 $^{\circ}$)	200	1.7	488.225
IRAS 18151–1208	0. $''$ 099 \times 0. $''$ 057 (86 $^{\circ}$)	230	1.3	488.228
IRAS 18162–2048	0. $''$ 082 \times 0. $''$ 067 (–86 $^{\circ}$)	100	1.4	488.225
IRAS 18182–1433	0. $''$ 107 \times 0. $''$ 057 (–87 $^{\circ}$)	280	1.4	488.229
IRAS 18337–0743	0. $''$ 111 \times 0. $''$ 090 (–40 $^{\circ}$)	380	2.2	488.285
IRDC 18223–1243	0. $''$ 102 \times 0. $''$ 058 (–89 $^{\circ}$)	260	1.3	488.227
NGC 6334I	0. $''$ 093 \times 0. $''$ 065 (75 $^{\circ}$)	110	1.9	488.286
NGC 6334I(N)	0. $''$ 095 \times 0. $''$ 066 (78 $^{\circ}$)	110	1.5	488.286
W33A	0. $''$ 081 \times 0. $''$ 061 (84 $^{\circ}$)	180	1.8	488.224

NOTE—Columns are the same as in Table 1, except for the distance column.

Table 3. Additional lines used from the 220 GHz spectral window

Source	Molecule	Transition	Rest Freq.	E_u/k_B	Beam	Res.
			(GHz)	(K)	maj \times min (P.A.)	(au)
G333.46–0.16	HNCO	$J_{K_a, K_c} = 10_{0,10} - 9_{0,9}$	219.79832	58	0. $''$ 115 \times 0. $''$ 076 (–33 $^{\circ}$)	270
IRAS 18162–2048	c-HCOOH	$J_{K_a, K_c} = 10_{4,6} - 9_{4,5}$	219.9729675	116	0. $''$ 082 \times 0. $''$ 066 (–89 $^{\circ}$)	100
NGC 6334I	HNCO	$J_{K_a, K_c} = 10_{3,8} - 9_{3,7}$	219.6567695	433	0. $''$ 096 \times 0. $''$ 065 (76 $^{\circ}$)	110

NOTE—The molecular line transitions assigned to the line emission are tentative. Noise levels and channel widths per source are the same as in Table 2.

ertheless, we keep these sources to further analyze their emission and kinematics through position-velocity (PV) maps. A few fields have extended emission covering several cores cataloged in Paper IV where it is not possible to assess if the emission belongs to a specific source, and thus we exclude these sources in the analysis. These

cases include G5.89–0.37, where part of the emission is associated with an H II region, and NGC 6334I where extended emission is found to be connecting different sources. Similarly, for W33A, we found that the kinematics associated with the object labeled as ALMAe4 could only be partially separated from the cloud emission.

Table 4. Source detections

Source	ALMAe	Mol.	R. A.	Decl.	v_{LSR}	P.A.	Out. P.A.	P.A.
	Source		[$h:m:s$]	[$^{\circ}:':":'$]	(km s^{-1})	(deg)	(deg)	Ref.
	(1)	(2)	(3)	(4)	(5)	(6)	(7)	(8)
G10.62–0.38	1	CH ₃ CN	18 : 10 : 28.60755	−19 : 55 : 49.4614	0.85	0
	2	CH ₃ CN	18 : 10 : 28.69080	−19 : 55 : 49.8281	−1.51	−30
	3	CH ₃ CN	18 : 10 : 28.73003	−19 : 55 : 49.4837	−1.35	180
G11.1–0.12	1	CH ₃ CN	18 : 10 : 28.24854	−19 : 22 : 30.3222	31.85	−65
G11.92–0.61	1	CH ₃ CN	18 : 13 : 58.11097	−18 : 54 : 20.2010	35.1	129	53	[1]
	4	CH ₃ CN	18 : 13 : 58.13491	−18 : 54 : 16.2731	35.7	225
	6	CH ₃ CN	18 : 13 : 58.12719	−18 : 54 : 20.7199	37.0	−15
G14.22–0.50 S	3	CH ₃ OH	18 : 18 : 12.86247	−16 : 57 : 20.3666	22.0	170	75	...
G29.96–0.02	1	CH ₃ OH	18 : 46 : 03.77860	−02 : 39 : 22.3746	97.25	155 ^b	142	[2]
G333.12–0.56	1	CH ₃ OH	16 : 21 : 35.37589	−50 : 40 : 56.6044	−58.47	135	40	...
	8	CH ₃ CN	16 : 21 : 36.25475	−50 : 40 : 47.2340	−54.10	90	−35	...
	6	CH ₃ CN	16 : 19 : 50.88363	−50 : 15 : 10.5272	−87.04	220	133 ^c	[3]
G333.23–0.06	17	CH ₃ CN	16 : 19 : 50.87824	−50 : 15 : 10.6063	−87.04	125	221 ^c	[3]
	1	HNCO	16 : 21 : 20.17674	−50 : 09 : 46.3768	−43.55	130	100	...
	2	CH ₃ CN	16 : 21 : 20.17290	−50 : 09 : 48.8762	−43.2	130	209	[4]
G335.579–0.272	1	CH ₃ OH	16 : 30 : 58.76705	−48 : 43 : 53.8816	−46.9	150	240	[5]
	4	CH ₃ OH	16 : 30 : 58.63085	−48 : 43 : 51.2159	−53.1	202	−72	[6, 7]
	1	CH ₃ OH	16 : 29 : 47.33461	−48 : 15 : 52.2666	−48.94	215	−30	...
G335.78+0.17	2	CH ₃ OH	16 : 29 : 46.12974	−48 : 15 : 49.9512	−50.51	65
	3	CH ₃ OH	16 : 35 : 09.25854	−48 : 46 : 47.6623	−47.2	125	205	[8]
	2	CH ₃ OH	18 : 53 : 18.00684	+01 : 25 : 25.4228	58.44	280	200	...
G343.12–0.06	1	CH ₃ OH	16 : 58 : 17.20735	−42 : 52 : 07.4161	−33.71	230	135	[9, 10]
G35.03+0.35 A	1	CH ₃ CN	18 : 54 : 00.65099	+02 : 01 : 19.3410	45.94	310	110	...
G35.13–0.74	1	CH ₃ CN	18 : 58 : 06.13626	+01 : 37 : 07.4306	35.93	45	145	...
	2	CH ₃ CN	18 : 58 : 06.16874	+01 : 37 : 08.1602	34.39	75
	7	CH ₃ CN	18 : 58 : 06.27972	+01 : 37 : 07.2029	35.53	95	0	...
G35.20–0.74 N	1	CH ₃ OH	18 : 58 : 12.95261	+01 : 40 : 37.3652	32.11	−10 ^d	30	[11]
	2	CH ₃ OH	18 : 58 : 13.03690	+01 : 40 : 35.9257	30.0	−23	3	[11, 12]
G351.77–0.54	2	CH ₃ OH	17 : 26 : 42.53329	−36 : 09 : 17.3878	−3.83	130	−24	[13, 14]
G5.89–0.37	1	CH ₃ CN	18 : 00 : 30.63209	−24 : 04 : 03.0057	7.92	−30
IRAS 16562–3959	1	CH ₃ CN	16 : 59 : 41.62564	−40 : 03 : 43.6385	−16.86	10	100	[15]
	5	CH ₃ CN	16 : 59 : 41.08769	−40 : 03 : 39.0848	−11.65	225	285	...
IRAS 18089–1732	1	CH ₃ CN	18 : 11 : 51.45454	−17 : 31 : 28.8163	32.88	245	−12 ^e	...
	2	CH ₃ CN	18 : 11 : 51.39962	−17 : 31 : 29.9457	33.02	315	35	...
IRAS 18162–2048	1	c-HCOOH	18 : 19 : 12.09528	−20 : 47 : 30.9566	45.69	−70	20	[16, 17]
IRAS 18182–1433	1	CH ₃ CN	18 : 21 : 08.97822	−14 : 31 : 47.5970	60.64	0	90	...
	2	CH ₃ CN	18 : 21 : 09.04928	−14 : 31 : 47.7925	62.78	40	155	...
	5	CH ₃ CN	18 : 21 : 09.12462	−14 : 31 : 48.5998	61.12	10	130	...
	11	CH ₃ CN	18 : 21 : 09.01613	−14 : 31 : 47.9401	62.7	40
NGC 6334 I	1	HNCO	17 : 20 : 53.41869	−35 : 46 : 57.8969	−8.0	60	0	...
	3	CH ₃ OH	17 : 20 : 53.64398	−35 : 46 : 54.8823	−4.7	50
	4	HNCO	17 : 20 : 53.16652	−35 : 46 : 59.1704	−6.92	20	250	...

Table 4 *continued*

Table 4 (continued)

Source	ALMAe	Mol.	R. A.	Decl.	v_{LSR}	P.A.	Out. P.A.	P.A.
	Source		[$h : m : s$]	[$^{\circ} : ' : ''$]	(km s^{-1})	(deg)	(deg)	Ref.
		(1)	(2)	(3)	(4)	(5)	(6)	(7)
NGC 6334I(N)	1	CH ₃ OH	17 : 20 : 54.59280	-35 : 45 : 17.3686	-3.9	-55
	2	CH ₃ OH	17 : 20 : 55.19138	-35 : 45 : 03.9525	-1.77	310	35	...
	8	CH ₃ CN	17 : 20 : 54.61962	-35 : 45 : 08.6715	-7.2	130
	9	CH ₃ CN	17 : 20 : 54.87122	-35 : 45 : 06.4309	-6.7	130	40	...
	14	CH ₃ CN	17 : 20 : 54.83871	-35 : 45 : 06.0527	-5.0	160
W33A	1	CH ₃ CN	18 : 14 : 39.51004	-17 : 52 : 00.1338	37.9	-30	120	[18]
	4	CH ₃ CN	18 : 14 : 39.52227	-17 : 52 : 00.4500	37.9	90

NOTE—(1) Extended configuration condensation index. (2) Molecule analyzed. (3) & (4) Continuum position in ICRS system. (5) Systemic velocity. (6) Velocity gradient P.A. (east from north) as shown in the first order moment map in Figure 1. (7) Outflow direction P.A. (8) Reference for the P.A. of the velocity gradient, the outflow or both as specified in the Table References. Note that some outflow angles are not quoted in the references, but they are measured from the observations presented there.

^aC. J. Cyganowski et al. (2011) lists an outflow that may be associated to this source, however we could not determine its P.A.

^bR. Cesaroni et al. (2017) used a P.A. orthogonal to the outflow direction. However A. Sanchez-Monge (2019) showed that there is an accretion flow close to the outflow axis.

^cS. Li et al. (2024) found several outflow candidates in this region using DIHCA compact configuration data (angular resolution $\sim 0.^{\circ}5$), here we assign them based on the direction with respect to the CH₃CN velocity gradient.

^dÁ. Sánchez-Monge et al. (2014) derived a P.A. of 10° while Y. Zhang et al. (2022) used a value of 0°, the value in the table is more appropriate from the first moment map in Figure 1.

^eH. Beuther et al. (2004) found a P.A. of roughly 20° from SiO emission at $\sim 2''$ resolution, while SiO emission at $\sim 0.^{\circ}5$ resolution from DIHCA favors a slightly eastern direction.

References— [1] J. D. Ilee et al. (2018); [2] outflow: R. Cesaroni et al. (2017); [3] outflow: S. Li et al. (2024); [4] outflow: P. Saha et al. (2024); [5] Paper II; [6] rotation: Paper I; [7] outflow: A. Avison et al. (2021); [8] F. A. Olgun et al. (2023); [9] rotation: K. E. I. Tanaka et al. (2020); [10] outflow: L. A. Zapata et al. (2019); [11] outflow: Y. Zhang et al. (2022); [12] rotation: Á. Sánchez-Monge et al. (2014); [13] rotation: A. Ginsburg et al. (2023); [14] outflow: H. Beuther et al. (2019); [15] A. E. Guzmán et al. (2020); [16] rotation: N. Añez-López et al. (2020); [17] outflow: C. Carrasco-González et al. (2012); [18] outflow: L. T. Maud et al. (2017).

Fig. Set 1. First order moment maps

3.2. Source kinematics

Of the 49 sources with line emission, most exhibit velocity gradients as shown in the first moment maps in Figure 1. These moment maps were produced from emission over the 5σ level. The direction of the velocity gradients was determined visually from the first moment maps and channel-by-channel, but informed by the discrete first derivative of the first moment maps around the sources and the continuum morphology, for the sources whose rotation direction is not in the literature (Table 4). To confirm that the gradient directions are likely those of a disk-outflow system, Figure 1 shows the direction of the outflows in the literature (see Table 4 for the references) or the tentative directions from DIHCA SiO $J = 5 - 4$ data. A 60% of the sources with (tentative) outflow detections (33 sources) have gradient-outflow angles within 20° of the expected for disk-outflow systems (i.e., 90° \pm 20°). This fraction in-

creases to 80% for the 90° \pm 45° range. Note that some of the directions of velocity gradients in the literature are chosen to be orthogonal to the outflow direction. For G335.579-0.272 ALMAe1 we use the gradient direction from Paper II, which better represents the rotation close to the main source as traced by vinyl cyanide (CH₂CHCN) emission. Á. Sánchez-Monge et al. (2014) derived a P.A. of 10° for G35.20-0.74 N ALMAe1 while Y. Zhang et al. (2022) favors a P.A. of 0°. Here we use a P.A. of -10°, which follows closer the orientation of the continuum elongation. The kinematics in G351.77-0.54 are rather complex and the position angle uncertain due to possible contamination from molecular line emission in the outflow (H. Beuther et al. 2017). Thus, we list the position angle of ALMAe2 derived from the disk traced by salts (e.g., A. Ginsburg et al. 2023), while the large scale velocity gradient is closer to the east-west direction (e.g., H. Beuther et al. 2025b). Finally, the position angle from A. E. Guzmán et al. (2020) for IRAS 16562-3959 ALMAe1 was derived from rotation traced by hydrogen recombination lines. Its orientation is or-

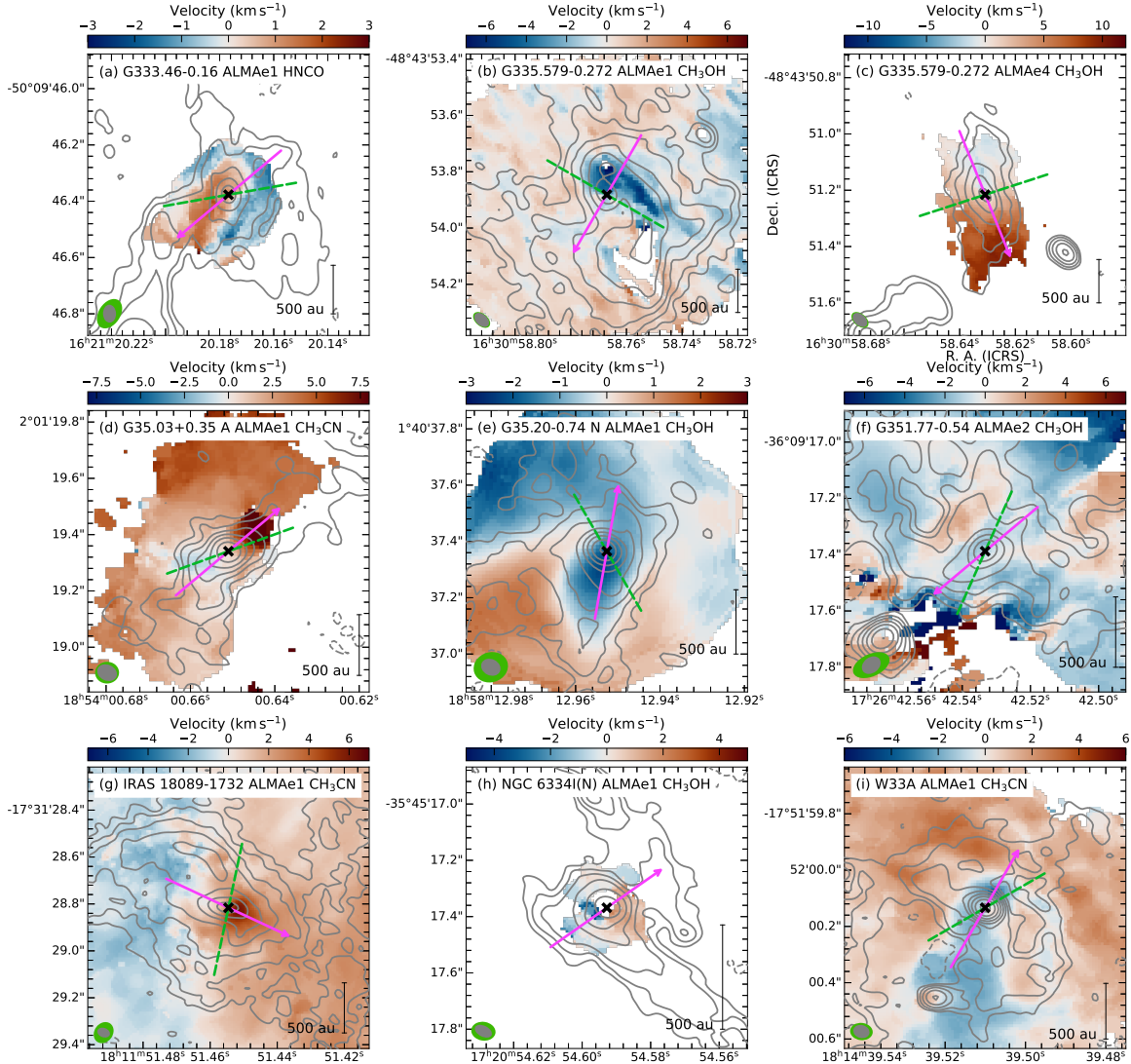


Figure 1. First order moment maps from the labeled molecule emission (color scale) and continuum emission (contours) of the detected condensations. The contour levels are $5, 10, 20, \dots \times \sigma$ where σ is the noise level estimated as the standard deviation from the median absolute deviation of the continuum maps. The black crosses mark the position of the condensations in Table 4, while the pink arrows show the direction of the velocity gradient used to calculate the position-velocity maps in Figure 2. The green dashed lines show the direction of the (tentative) outflows. The synthesized beam of the continuum (gray ellipse) and the moment maps (green ellipse; see Tables 1-3) are shown in the bottom left corner. The complete figure set (48 images) is available in the online journal.

thogonal to that of the gradient detected in CH₃CN, however, this may be the result of CH₃CN contamination in the outflow cavities or significant misalignment of the rotation direction from the large envelope to the small scale ionized disk (e.g., M. R. Bate 2018).

To confirm the rotation nature of the first moment maps, we produce PV maps along (pink arrows in Figure 1) and across the velocity gradients, with an slit width of 0''.05 (this is the expected resolution of the continuum, and corresponds to 5 pixels). The PV maps are presented in Figures 2 and 3. To facilitate the modeling below, we orient the slits from blue- to red-shifted emis-

sion, i.e., the arrows in Figure 1 are oriented toward the P.A. in Table 4 from the source position. Figure 2 shows the PV maps whose velocity gradient can be modeled as a power law (32 sources, see below). These velocity gradients show distributions resembling Keplerian-like rotation (e.g., IRAS 18089-1732 ALMAe1) and rotation with infall (e.g., G335.579-0.272 ALMAe1) rather than outflows. Most strikingly, many sources (around a third) show asymmetric PV maps with a lobe approximately Keplerian and another that is not. These asymmetries are also expressed in the form of different peak intensity between lobes. We count 14 sources where the blue-

shifted lobe dominates, 7 sources where the red-shifted lobe dominates and 11 sources where neither lobe dominates. The possible origins for these asymmetries is discussed in § 4.1. The sources that do not show clear or resolved velocity gradients, or with velocity gradients resembling solid body rotation ($v \propto r$) are presented in Figure 3. On the other hand, the PV maps in the orthogonal direction allow the identification of possible infall and outflow motions.

Fig. Set 2. PV maps with fitted edge

Fig. Set 3. PV maps without edge

In order to obtain the physical properties of the condensations (e.g., central source masses) we derive the edge of the PV on each lobe (e.g., Y. Aso et al. 2015; D. Seifried et al. 2016; J. Sai et al. 2020). Here, the edge is defined as the points at a certain contour level (see Appendix B for details on contour selection). To derive the edge offset corresponding to each velocity value, we first find the offset with the closest intensity to the selected contour level (initial offset). Then we perform an intensity weighted average of pixels around the initial offset. For this average we use a total of 5 offset values centered in the initial offset (i.e., 2 values on each side). Similar to Y. Aso et al. (2015), we fit a power law to the velocity along the line of sight, v_{los} , as a function of the offset, θ , of the form:

$$v_{los} = v_{sys} + \begin{cases} -v_{100} \left(\frac{|\theta - \theta_{off}|}{100 \text{ au}} \right)^\alpha & \text{if } \theta < \theta_{off} \\ v_{100} \left(\frac{\theta - \theta_{off}}{100 \text{ au}} \right)^\alpha & \text{if } \theta \geq \theta_{off} \end{cases}, \quad (1)$$

where v_{100} is the velocity at 100 au, and v_{sys} and θ_{off} determine the zero velocity and offset values, respectively. In this definition, a Keplerian disk would have a power law index $\alpha = -0.5$. Note that free-fall also has a power law index of -0.5 but the velocity gradient in the orthogonal direction of the PV map is expected to follow the same distribution, while pure rotation should be flat as the velocity along the line of sight should be zero in the orthogonal direction. For a rotating and infalling envelope under specific angular momentum conservation an α value of -1 is expected (e.g., Y. Oya et al. 2022). The fitting is performed in three steps, first we fit an initial Keplerian distribution with initial parameters from the data and a restricted θ_{off} value between the closest points where the distribution changes to the opposite quadrant. Without this first step solutions tend to diverge for some sources in the following steps. The results are then used as initial parameters for a fit with all parameters free and without boundary conditions, henceforth referred to as the boundless fit. Finally, we perform a final Keplerian fit (α set to -0.5) with only the velocity v_{100} as a free parameter and the remaining pa-

rameters (v_{sys} and θ_{off}) set to the boundless fit results. We successfully fitted the edges of 32 sources ($\sim 60\%$ of the sources with line detection) and the results of the fit are listed in Table 5. The first Keplerian fit is performed using the Sequential Least Squares Programming fitter from `astropy`, which allows for boundary conditions for the input parameters. The latter two fits are performed using the Orthogonal Distance Regression fitter from `scipy`, which allow for data with errors in both axes. In this case, we estimate the error in offset from the propagation of uncertainty for the weighted average with an error per pixel equal to the beam size (geometric mean in Gaussian dispersion form). The error in velocity is one channel, i.e., half the velocity resolution. The error values in Table 5 are the standard deviation of the fitted parameters calculated by the regression algorithm. From the Keplerian power law, we estimate an enclosed mass within 100 au and uncorrected for source inclination from the fit results:

$$M_c \sin^2 i = 100 \text{ au} \frac{v_{100}^2}{G}, \quad (2)$$

with G the gravitational constant. We use v_{100} from the Keplerian fit, which is not the best for all sources. Particularly for sources with $\alpha = -1$, infall and rotation cannot be separated from just the direction of the velocity gradient alone and the equivalent $M_c \sin^2 i$ would need to fit both PV slit directions (e.g., M. Momose et al. 1998). The errors in mass are derived from the propagation of uncertainty. Note that by fitting the edge of the PV maps the masses will be overestimated compared to fitting the peak intensity (the so-called ridge; e.g., J. Sai et al. 2020). The anisotropic nature of the PV morphologies and/or non-Gaussian line shape precludes a good ridge fitting. Since the ridge includes emission from the bulk of the envelope, the measured power law from the PV maps can have contamination leading to a shallower index (S. Mori et al. 2024). For instance, the central source mass can be overestimated by a factor ~ 2 if Keplerian rotation is assumed but the underlying velocity distribution follows that of a infalling and rotating envelope under specific angular momentum conservation.

In general relatively good fits are obtained by the boundless power law fit. Figure 4(a) shows a histogram of the alpha values without outliers ($\alpha < -2$) binned using the Freedman Diaconis estimator. The histogram peaks around an α value of -0.6 . Some of the α values are close to Keplerian (e.g., G333.46–0.16 ALMAe2), while others seem to follow rotation under specific angular momentum conservation power law (e.g., G335.78+0.17 ALMAe1). We group the sources by using α ranges (color coded in Figure 2): $\alpha > -0.7$ for Ke-

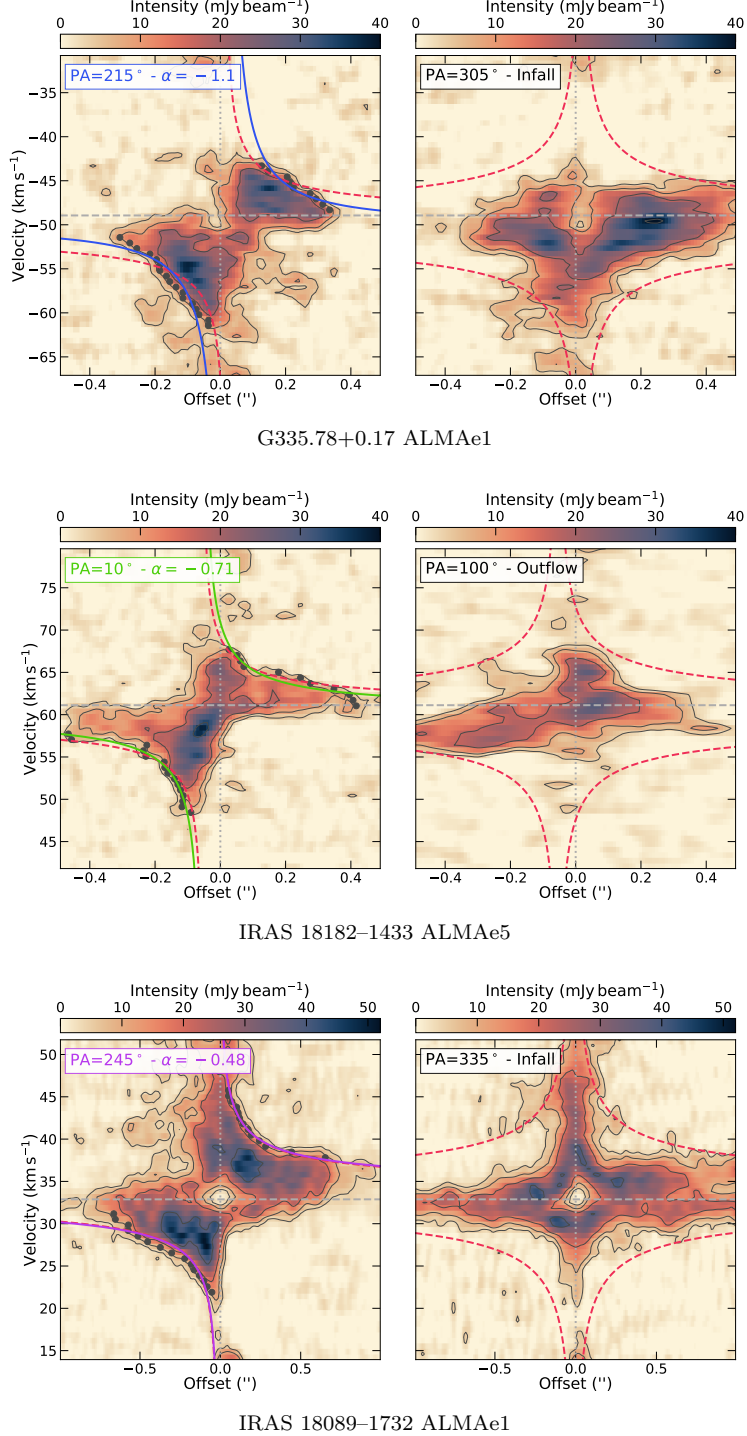
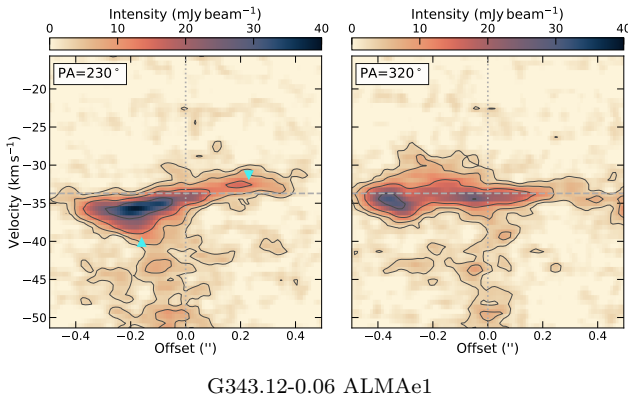


Figure 2. Position velocity maps along (left) and orthogonal (right) to the velocity gradient direction for each condensation with edge calculation. The molecular line emission used for the maps is listed in Table 4 (see also Figure 1). Left: The black dots mark the edge points, and the continuous colored line and dashed red line show the boundless and Keplerian power law fits to the edge points, respectively (see §3.2). The colored lines and labels group sources in those with $\alpha > -0.7$ (purple), $-0.7 \geq \alpha \geq -0.8$ (green), $\alpha \leq -0.8$ (blue) and outliers ($\alpha < -2$, black). Right: The red dashed lines correspond to a free-fall velocity profile, i.e., $\sqrt{2}$ times the Keplerian power law in the left panel. Note that these are plotted in the four quadrants because the location of the closest half of the disk is unknown along the PV slit. Profiles resembling infall (blue skewed or inverse p-Cygni) or outflows (e.g., Hubble-like expansion) are labeled. The dotted vertical and dashed horizontal gray lines indicate the zero position offset and the systemic velocity (Table 4), respectively. The complete figure set (32 images) is available in the online journal.



G343.12-0.06 ALMAe1

Figure 3. Position velocity maps along and orthogonal to the velocity gradient direction for each condensation where the edge could not be determined. The cyan triangles indicate the position of the velocity extrema determined from the edge points. The dotted vertical and dashed horizontal gray lines indicate the zero position offset and the systemic velocity (Table 4), respectively. The complete figure set (17 images) is available in the online journal.

plerian, $-0.8 \leq \alpha \leq -0.7$ for mixed and $\alpha < -0.8$ as infall and rotation under angular momentum conservation. Values between -0.5 and -1 can be the result of changes in α with radius as expected from the transition from envelope to disk (e.g., G11.92–0.61 ALMAe1), unresolved disks embedded in an envelope, or asymmetric distributions of the edges at opposite lobes (e.g., G35.03+0.35 A ALMAe1). Sources G10.62–0.38 ALMAe1, G11.92–0.61 ALMAe1, G29.96–0.02 ALMAe1, G333.12–0.56 ALMAe1, G335.579–0.272 ALMAe1, G5.89–0.37 ALMAe1, IRAS 18089–1732 ALMAe1, NGC 6334I(N) ALMAe8 and ALMAe9, and W33A ALMAe1 have PV maps that are similar in both slit directions and could also be fitted by a power law, hence in these cases a contribution from infall (e.g., $\alpha = -1$ for a rotating and infalling envelope Y. Oya et al. 2022) is expected in the measured α values. As a guide, the right panels of Figure 2 show the expected curve from free-fall for a source with the same mass derived from the Keplerian assumption, i.e., the free-fall velocity at 100 au is $v_{100,ff} = \sqrt{2}v_{100}$ with v_{100} from the Keplerian fit. We classify the PV maps in the orthogonal direction on whether they resemble outflows (Hubble-like expansion $v_{los} \propto r$) or infall profiles (blue skewed profiles or inverse p-Cygni). Figure C1 in Appendix C shows the peak spectra toward the 32 sources to confirm the infalling nature of some of the sources in the sample. Of the sources with large α values, G11.1–0.12 ALMAe1 seems to follow a power law in one lobe while the other lobe has a complex intensity distribution that precludes a good fit. G336.01–0.82 ALMAe3 is also not well fitted by a power law distribution, however, the detailed modeling presented in F. A. Olgún et al. (2023)

shows that the emission can be well described by a rotating and infalling envelope.

As shown in the first moment maps (Figure 1), many sources are embedded in extended line emission from the surrounding clouds (e.g., G10.62–0.38 ALMAe2), making it difficult to disentangle the kinematics of the individual condensations. In addition to the sources whose kinematics cannot be resolved, we obtain an upper limit for the source mass from their PV map distribution. For these sources we apply the same algorithm to derive the edge, but select one (e.g., when the individual gas kinematics cannot be disentangled from the cloud) or two (e.g., when the kinematics cannot be fitted by a power law) points which represent the maximum line of sight velocity v_{los} . These sources are listed in Table 6 and the points are represented by triangles in Figure 3. Assuming that the infall and rotation contribution is the same, the upper limit of the mass of the source within a radius r can be calculated as (Y. Oya et al. 2014):

$$M_c \sin^2 i = \frac{r}{G} \Delta v^2, \quad (3)$$

where Δv is either $|v_{los} - v_{LSR}|$ for sources with only one measurement and $|v_{los,1} - v_{los,2}|/2$ otherwise. Similarly, the radius for sources with one measurement is the distance to zero offset, while for those with two measurements is half the distance between both measurements. The latter choice is justified by the fact that many of the sources are asymmetric and that the v_{LSR} may not be well estimated.

4. DISCUSSION

4.1. Anisotropic collapse

The PV maps presented in Figure 2 show a variety of rotation curves. They show intensity distributions that are not as smooth as some of those detected toward low-mass disks (e.g., Y. Aso et al. 2015). These asymmetries result in PV maps seemingly having two different distributions on opposite sides (expressed in power laws fitting one side better than the other), one side brighter than the other, and/or shifts in offset from the continuum source position. The observed intensity is an interplay of density distribution and temperature gradient in the system. In the case of a hot disk embedded in a colder collapsing envelope, a weaker red-shifted lobe in the PV map is expected due to absorption caused by receding colder gas in the near side of the envelope (e.g., H.-R. V. Chen et al. 2016). However, such a simple model cannot account for cases with a stronger red-shifted lobe. We speculate that anisotropic infall occurs in more than half of our sample. Anisotropic collapse can be the result of the initial turbulence and magnetic

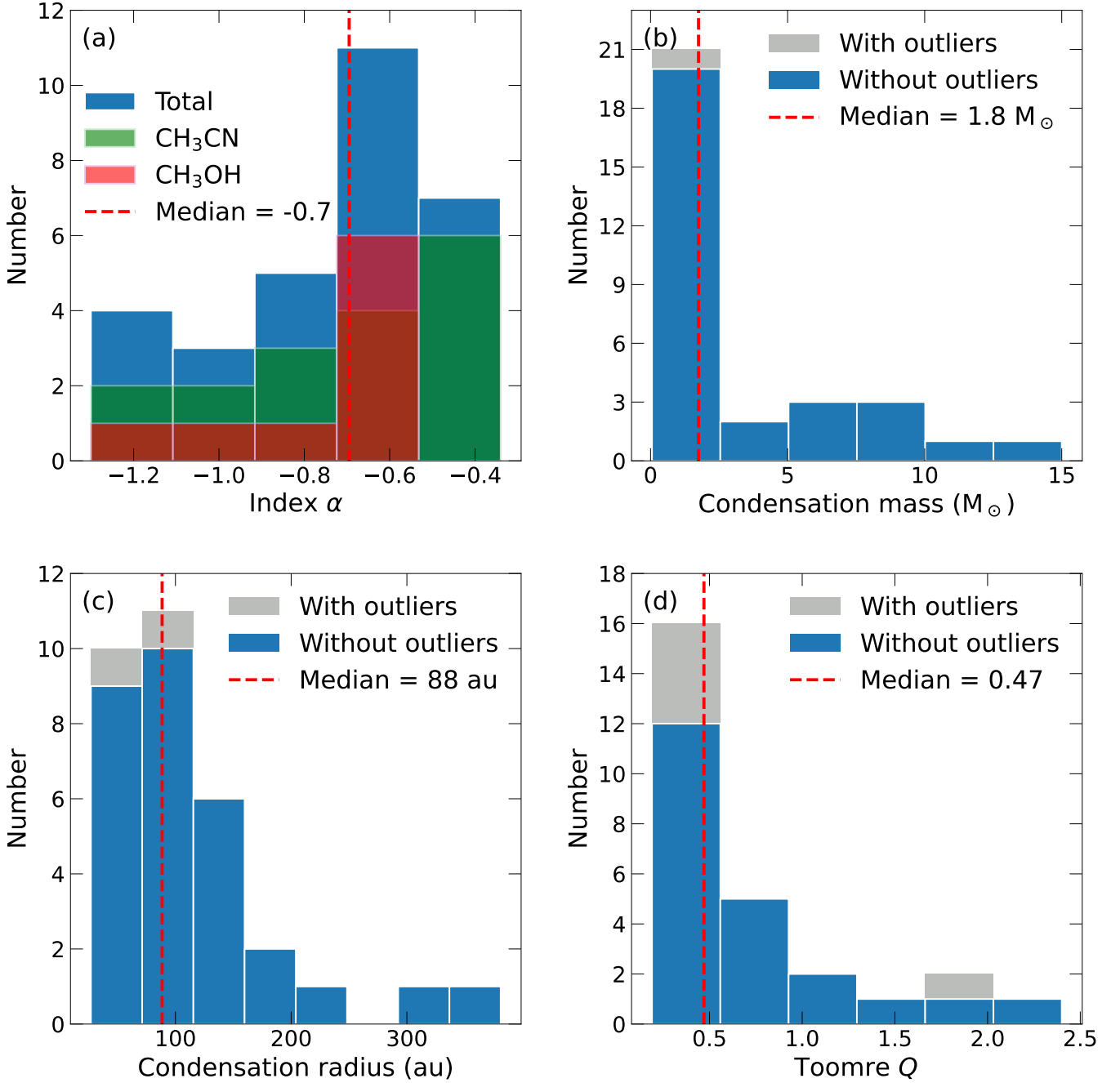


Figure 4. Histograms of (a) power law indices α values, (b) condensation masses, (c) condensation radii and (d) Toomre- Q parameter. Outliers with $\alpha < -2$ are not considered in (a), while the outliers for the other parameters are defined in §4.2. A further outlier source in (b) is located at $40 M_{\odot}$, while two additional sources in (d) are located at 3.1 and 12 (see Table 7). Note that in (a) the total include three sources studied in other lines than CH_3OH and CH_3CN .

Table 5. PV map edge fitting and central source masses

Source	ALMAe		Boundless			Keplerian	
	Source	α	v_{100}	v_{sys}	θ_{off}	v_{100}	$M_c \sin^2 i$
			(km s $^{-1}$)	(km s $^{-1}$)	(mas)	(km s $^{-1}$)	(M $_{\odot}$)
G10.62–0.38	1	-1.2 ± 0.5	36 ± 25	-2.3 ± 0.9	82 ± 9	12 ± 1	16 ± 3
	3	-1.0 ± 0.2	14 ± 4	-2.2 ± 0.3	41 ± 9	6.6 ± 0.5	5.0 ± 0.8
G11.1–0.12	1	-3 ± 1	120 ± 170	27.5 ± 0.8	66 ± 13	7.8 ± 0.8	7 ± 2
G11.92–0.61	1	-0.91 ± 0.05	43 ± 4	35.1 ± 0.2	10 ± 6	19.9 ± 0.7	45 ± 3
	4	-0.58 ± 0.07	11 ± 1	36.0 ± 0.2	-7 ± 8	9.9 ± 0.3	11.0 ± 0.6
G29.96–0.02	1	-0.77 ± 0.08	37 ± 7	97.8 ± 0.3	16 ± 11	19.9 ± 0.9	45 ± 4
G333.12–0.56	1	-0.56 ± 0.06	13 ± 1	-58.1 ± 0.2	-36 ± 7	11.6 ± 0.2	15.2 ± 0.6
G333.23–0.06	6	-0.86 ± 0.07	18 ± 2	-87.5 ± 0.2	28 ± 4	10.1 ± 0.5	11 ± 1
	17	-1.2 ± 0.4	20 ± 10	-87.7 ± 0.5	24 ± 8	7.6 ± 0.8	7 ± 1
	1	-0.8 ± 0.1	10 ± 1	-43.6 ± 0.3	32 ± 9	6.9 ± 0.4	5.4 ± 0.6
G335.579–0.272	2	-0.45 ± 0.05	9.5 ± 0.6	-41.8 ± 0.2	-18 ± 8	10.1 ± 0.3	11.6 ± 0.6
	1	-0.62 ± 0.06	9.4 ± 0.7	-46.5 ± 0.2	-23 ± 5	8.2 ± 0.3	7.6 ± 0.5
G335.78+0.17	4	-0.64 ± 0.05	21 ± 2	-48.8 ± 0.2	45 ± 6	16.6 ± 0.3	31 ± 1
	1	-1.1 ± 0.1	33 ± 8	-50.0 ± 0.3	15 ± 11	12.2 ± 0.7	17 ± 2
G336.01–0.82	2	-0.7 ± 0.2	12 ± 3	-51.6 ± 0.5	11 ± 15	9.3 ± 0.6	10 ± 1
	3	-2.1 ± 0.5	180 ± 150	-45.4 ± 0.6	4 ± 15	11 ± 1	14 ± 3
G34.43+0.24 MM1	2	-0.58 ± 0.08	16 ± 3	58.7 ± 0.2	-21 ± 16	13.9 ± 0.4	22 ± 1
G35.03+0.35 A	1	-0.7 ± 0.4	18 ± 10	51 ± 2	-20 ± 50	13.3 ± 0.7	20 ± 2
	1	-0.46 ± 0.06	7.5 ± 0.5	35.8 ± 0.2	-38 ± 8	7.7 ± 0.2	6.8 ± 0.4
G35.13–0.74	2	-1.0 ± 0.4	6 ± 1	34.0 ± 0.7	-14 ± 15	4.9 ± 0.3	2.7 ± 0.4
	1	-1.2 ± 0.2	15 ± 5	31.8 ± 0.3	-34 ± 20	5.9 ± 0.6	3.9 ± 0.8
G35.20–0.74 N	1	-0.4 ± 0.1	8 ± 2	8.2 ± 0.4	33 ± 24	8.6 ± 0.8	8 ± 2
IRAS 18089–1732	1	-0.48 ± 0.04	15.3 ± 0.8	33.5 ± 0.2	-10 ± 8	15.6 ± 0.3	28 ± 1
	2	-0.80 ± 0.09	11 ± 1	33.2 ± 0.3	1 ± 7	8.1 ± 0.4	7.5 ± 0.7
IRAS 18162–2048	1	-0.34 ± 0.09	8.8 ± 0.8	44.3 ± 0.4	20 ± 40	10.3 ± 0.3	11.9 ± 0.6
IRAS 18182–1433	5	-0.71 ± 0.06	17 ± 2	60.2 ± 0.2	-54 ± 7	12.4 ± 0.4	17 ± 1
NGC 6334I	1	-0.6 ± 0.1	10 ± 2	-6.5 ± 0.3	-4 ± 30	8.8 ± 0.5	8.7 ± 0.9
	4	-1.3 ± 0.2	24 ± 6	-8.1 ± 0.2	13 ± 17	8.1 ± 0.7	7 ± 1
NGC 6334I(N)	2	-0.6 ± 0.2	13 ± 3	-3.6 ± 0.5	120 ± 40	10.9 ± 0.5	13 ± 1
	8	-0.44 ± 0.05	9.1 ± 0.4	-3.7 ± 0.2	-33 ± 9	9.4 ± 0.2	10.0 ± 0.5
	9	-0.69 ± 0.08	7.5 ± 0.5	-5.1 ± 0.3	3 ± 10	6.7 ± 0.3	5.0 ± 0.4
W33A	1	-0.53 ± 0.06	13 ± 1	37.3 ± 0.3	16 ± 9	12.6 ± 0.5	18 ± 2

Table 6. PV map edge extrema

Source	ALMAe	Δv	r	$M_c \sin^2 i$
	Source	(km s ⁻¹)	(au)	(M _⊕)
G11.92-0.61	6	4.0	233	4
G14.22-0.50 S	3	4.1	88	2
G333.12-0.56	8	4.7	310	8
G343.12-0.06	1	4.4	570	12
G35.13-0.74	7	4.7	170	4
G35.20-0.74 N	2	3.5	380	5
IRAS 16562-3959	5	2.7	110	0.9
IRAS 18182-1433	1	3.3	200	3
	2	2.7	170	1
	11	3.0	64	0.6
NGC 6334I	3	2.5	68	0.5
NGC 6334I(N)	1	4.1	180	3
	14	5.1	120	3
W33A	4	6.0	430	18

field in these regions, which would allow the formation of structures like infall streamers (e.g., [D. Seifried et al. 2015](#)) as those confirmed in some of the sources in the sample (see next paragraph). A clumpy environment can also result in anisotropic collapse, as tidal events disrupts these gas clumps allowing the formation of asymmetric configurations (e.g., [C. P. Dullemond et al. 2019](#)). As these flows feed the midplane/disk defined by the rotation axis at different radius projected in the plane of the sky, the enhancement of density and/or temperature (e.g., due to accretion shocks) would result in asymmetric distributions of line emission and potentially dust continuum emission. In addition, since massive stars are frequently born in clustered environments ([H. Beuther et al. 2025a](#), and references therein), it is expected that core-core interactions are more frequent. These interactions or collisions result in shock-compressed gas allowing the formation of asymmetric streamers or gas stripping depending on the speed of the interaction (e.g., [Y. Yano et al. 2024](#)). Therefore the observed asymmetries can be in part the result of such interactions. Finally, the development of gravitational instabilities as a result of rapid infall can produce anisotropies within ~ 1000 au scales ([M. R. Krumholz et al. 2007a,b](#)).

For instance, the edges of sources like G335.78+0.17 ALMAe1 or NGC 6334I(N) ALMAe8 clearly show different slopes and probably different power law on either PV lobe. Most sources exhibit a brighter lobe (e.g., IRAS 18089-1732 ALMAe1 and ALMAe2), with some extreme cases where one lobe is much weaker (e.g., G35.03+0.35 A ALMAe1, also reported in [M. T. Beltrán et al. 2014](#)).

This has also been observed in other sources with asymmetrical gas distributions of rotating structures (e.g., IRAS 20126+4104 [R. Cesaroni et al. 2014](#), AFGL 4176 [K. G. Johnston et al. 2015](#)), and in the sample of [A. Ahmadi et al. \(2023\)](#) with the majority of its sources gravitationally unstable. These differences in intensity and potentially gas distributions are also detected in the continuum emission, which in most cases is asymmetric and, in some cases, with a distribution resembling spiral arms (the aforementioned streamers). Well-known examples of this in our sample are G336.01-0.82 ALMAe3, whose kinematics have been studied in detail as part of the DIHCA project ([F. A. Olgún et al. 2023](#)), IRAS 18089-1732 ALMAe1 ([P. Sanhueza et al. 2021](#)), IRAS 18162-2048 ALMAe1 ([M. Fernández-López et al. 2023](#)) and the streamer feeding the multiple system in W33A which includes ALMAe1 and ALMAe4 ([A. F. Izquierdo et al. 2018](#)). Those studies found that the (putative) disks are fed by streamers which can have different infall rates than the bulk of the envelope, thus explaining the differences in intensity/gas distribution.

In addition, a few sources show offsets between the position of the continuum source and the center of symmetry of the PV maps. One clear case is G335.579-0.272 ALMAe4, with an offset of roughly 50 mas (Table 5). This case seems to indicate that the high-mass source is not at the center of the disk/envelope either because it is part of a wide binary system or a previous core-core interaction with another source (second continuum peak seen in Figure 1). This is similar to the low-mass case IRAS 16293-2422 Source A ([Y. Oya & S. Yamamoto 2020](#)), where a forming multiple system produces a shift of the rotation centroid of the common envelope/disk. If the offset represents the position of the center mass of a potential binary system with respect to the primary and the mass in Table 5 is the total mass of the system, the primary and secondary stars would have a mass of roughly 27 and 4 M_⊕, respectively, for a plane of the sky distance of 355 mas (~ 1200 au) between them (measured from the continuum peak positions). An additional interpretation would be that the star is moving with respect to its natal cloud as a result of cluster dynamics, resulting in a shift of the source position with respect to the gas in its immediate surroundings and fed through Bondi-Hoyle-like accretion. On the other hand, G35.03+0.35 A ALMAe1 also has a slight offset of 20 mas, but in this case the reason seems to be filamentary accretion as proposed by [M. T. Beltrán et al. \(2014\)](#) and supported by the extended continuum emission toward the north-east (see Figure 1).

Table 7. Disk candidates properties

Source	ALMAe	T	L_{core}	$S_{1.3\text{mm}}$	$I_{1.3\text{mm}}$	$\tau_{1.3\text{mm}}$	R	M_g	Σ	Toomre Q	Disk
		(K)	(L_{\odot})	(mJy)	(mJy)		(au)	(M_{\odot})	($\times 10^2 \text{ g cm}^{-2}$)		motion
G10.62–0.38	1	202	4.1×10^5	155.7	13.9	1.1	149	40	51	0.07	Infall
	3	202	4.1×10^5	11.3	5.8	0.32	73	2.1	11	0.33	Infall
G11.1–0.12	1	62	3.4×10^2	4.4	1.4	0.26	100	1.0	2.9	0.47	Outlier
G11.92–0.61	1	212	7.9×10^3	55.8	11.3	0.84	149	5.8	7.4	0.47	Infall
	4	54 ^a	2.9×10^2	2.9	2.0	0.56	54	1.1	11	0.36	Keplerian
G29.96–0.02	1	270	1.4×10^5	90.6	16.0	0.47	217	15	9.1	0.27	Mixed
G333.12–0.56	1	193	1.4×10^3	56.5	12.0	0.88	133	6.3	10	0.25	Keplerian
G333.23–0.06	6	200	1.4×10^3	5.0	3.1	0.18	94	0.97	3.1	1.1	Infall
	17	200	1.4×10^3	2.4	1.4	0.077	< 106 ^b	0.44	1.1	1.9	Infall
G333.46–0.16	1	150	1.9×10^4	79.5	5.2	0.35	381	7.0	1.4	0.26	Mixed
	2	113	7.7×10^2	6.4	3.6	0.32	59	0.75	6.1	0.83	Keplerian
G335.579–0.272	1	250	1.5×10^4	29.4	17.6	1.2	65	2.8	19	0.31	Keplerian
	4	290 ^c	2.5×10^3	29.2	5.5	0.21	109	1.5	3.7	1.4	Keplerian
G335.78+0.17	1	250	8.3×10^3	116.4	20.8	1.5	156	12	14	0.19	Infall
	2	246	2.7×10^3	29.1	13.5	0.72	75	2.2	11	0.46	Mixed
G336.01–0.82	3	218	2.1×10^3	6.1	4.1	0.18	57	0.39	3.4	2.4	Outlier
G34.43+0.24 MM1	2	151	2.4×10^3	17.3	10.5	0.58	76	1.8	9.0	0.62	Keplerian
G35.03+0.35 A	1	218	3.4×10^3	9.8	9.2	0.29	< 63 ^b	0.37	2.6	3.1	Mixed
G35.13–0.74	1	100	7.8×10^2	44.8	19.5	...	70	2.9	17	0.19	Keplerian
	2	175	4.9×10^2	25.0	12.7	0.66	66	1.2	8.1	0.37	Infall
G35.20–0.74 N	1	202	9.0×10^3	91.3	31.2	2.6	81	8.0	35	0.12	Infall
G5.89–0.37	1	100	1.0×10^3	8.5	3.6	0.49	83	1.3	5.3	0.46	Keplerian
IRAS 18089–1732	1	247	1.5×10^4	109.5	20.1	2.2	114	7.9	17	0.27	Keplerian
	2	79	4.9×10^2	16.8	4.2	0.95	73	2.5	13	0.21	Mixed
IRAS 18162–2048	1	94	1.2×10^4	365.4	69.6	...	162	8.9	9.6	0.14	Keplerian
IRAS 18182–1433	5	278	3.0×10^3	38.6	3.2	0.1	312	2.4	0.7	1.1	Mixed
NGC 6334I	1	278 ^d	2.8×10^4	233.5	33.5	...	71	2.0	11	0.5	Keplerian
	4	400 ^d	1.1×10^4	8.4	7.0	0.18	32	0.054	1.5	12	Infall
NGC 6334I(N)	2	176	7.6×10^3	122.0	20.0	...	165	1.7	1.7	0.84	Keplerian
	8	201	4.0×10^2	38.7	9.7	0.64	130	0.62	1.0	1.8	Keplerian
	9	182 ^d	8.0×10^2	72.4	9.2	0.68	137	1.3	2.0	0.65	Keplerian
W33A	1	199	1.1×10^4	29.1	24.9	...	27	1.2	48	0.56	Keplerian

NOTE—Disk motion types are: “Infall” for infall and rotation under angular momentum conservation, “Keplerian” for those with power law $\alpha > -0.7$, “Mixed” for those with $-0.7 \geq \alpha \geq -0.8$, and “Outliers”. Fluxes are measured in the primary beam corrected continuum maps.

^a Brightness temperature (see Figure C1).

^b Beam size $(\sqrt{\theta_{\text{min}}\theta_{\text{max}}}/(2\sqrt{2\ln 2}))$ where θ values are the minor and major beam FWHM) at the source distance.

^c From Paper I.

^d From Paper V.

4.2. Scaling relationships

In this section we search for relations between different source parameters and other related quantities. To calculate the Spearman correlation coefficients, we exclude outlier values depending on the parameter or their combination. In addition to the aforementioned outliers in the power law index α values (see § 3.2, $\alpha < -2$), relations involving the central source mass $M_c \sin^2 i$ exclude close to face-on sources G335.579–0.272 ALMAe1 whose central mass is probably underestimated due to its inclination angle (Paper II), and G35.20–0.74 N ALMAe1, that also seem to be closer to

face-on (see shape of continuum and CH_3OH emission in Figure 1, and the masses determined from molecules other than CH_3OH and CH_3CN . The disk candidate radius, R , is derived from the deconvolved geometric mean of the semi-major and minor axes (FWHMs) of a 2-D Gaussian fitted during the source identification procedure utilizing PyBDSF (Paper VI), and individual values are listed in Table 7 and a histogram is shown in Figure 4(c). In relations involving the radius, we exclude G333.23–0.06 ALMAe17 and G35.03+0.35 A ALMAe1 whose deconvolved radius is undefined and instead we provide an upper limit defined by the beam size in Ta-

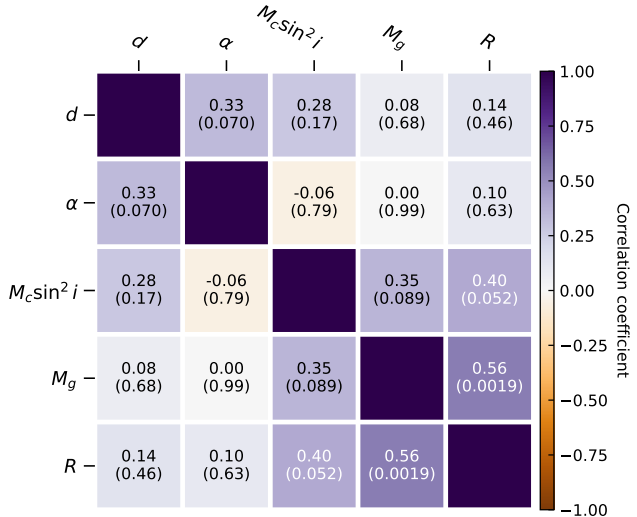


Figure 5. Correlations between selected source properties: distance d , power law index α , central source mass $M_c \sin^2 i$, disk candidate mass M_g , and disk candidate radius R . Spearman correlation coefficients and p-values (in parentheses) are calculated excluding outliers (see §4.2 for details).

ble 7. Finally, for relations involving the circumstellar gas mass and source luminosity (both described below), we exclude G10.62–0.38 ALMAe1 and ALMAe3 because they are likely contaminated by free-free emission.

Figure 5 summarizes the correlation coefficients between the parameters described above, except for the luminosity, without outliers. A very strong correlation has an absolute value of the Spearman coefficient between 0.8 and 1.0, a strong correlation between 0.6 and 0.79, a moderate correlation between 0.4 and 0.59, and weak and very weak correlations below 0.4. We only find (very) weak correlations between the distance and the source properties, but with relatively large p-values particularly for the gas mass and source radius. There is a moderate correlation between the source radius and the circumstellar gas mass (discussed below), while there is a borderline moderate correlation between the central source mass and the radius.

M. T. Beltrán & W. J. de Wit (2016) showed a correlation between the gas-to-stellar mass ratio, M_g/M_\star , and source radius derived from observations of intermediate and high-mass star-forming regions. They attributed this relation to the lack of enough angular resolution to separate disk and envelope components, and hence determine the nature of the rotation and the masses of the putative disks. From the flux densities of the condensations, S_ν , and peak continuum intensity, I_ν , measured by Paper VI and listed in Table 7, we estimate the circumstellar gas mass corrected for the optical depth (e.g.,

Y. Pouteau et al. 2022):

$$M_g = \tau_\nu \frac{\Omega_{\text{beam}} S_\nu d^2}{R_{dg} \kappa_\nu I_\nu} = \tau_\nu M_g^{\text{thin}} \frac{\Omega_{\text{beam}} B_\nu(T)}{I_\nu}, \quad (4)$$

with Ω_{beam} the beam area, d the distance in Table 4, $R_{dg} = 0.01$ the dust-to-gas ratio, B_ν the Planck black-body function, and M_g^{thin} the gas mass assuming optically thin emission. The optical depth is defined as

$$\tau_\nu = -\ln \left(1 - \frac{I_\nu}{\Omega_{\text{beam}} B_\nu(T)} \right). \quad (5)$$

We assume that the dust temperature is the same as the gas temperature estimated in Paper III by fitting the $^{13}\text{CH}_3\text{CN}$ $J_K = 13_K - 11_K$ K -ladder from the compact configuration DIHCA data. If the core associated to the condensation is not in Paper III we use the $^{13}\text{CH}_3\text{OH}$ rotational temperatures from Paper V, with the exception of G335.579–0.272 ALMAe4 where we use the temperature from Paper I. Note that the $^{13}\text{CH}_3\text{OH}$ temperatures are measured at the peak molecular line emission, hence we use the nearest value to the peak continuum emission. In the absence of any temperature measurement, we use the brightness temperature at the peak of the line (Figure C1). As the emission toward the central source becomes optically thick, the brightness temperature tends to the excitation temperature. Since complex organic molecules are detected in the sample, we expect that water ice is sublimated and the dust grains are bare silicates. Thus, we adopt a dust opacity value of $\kappa_\nu = 0.24 \text{ cm}^2 \text{ g}^{-1}$ at 1.3 mm, following R. Yamamoto et al. (2025), who evaluated the millimeter opacity of astronomical-silicate grains in massive protostellar disks using OPTOOL (C. Dominik et al. 2021). Sources G35.13–0.74 ALMAe1, IRAS 18162–2048 ALMAe1, NGC 6334I ALMAe1, NGC 6334I(N) ALMAe2 and W33A ALMAe1 have undefined τ_ν values. In these cases, we use the M_g^{thin} values.

The individual properties of each condensation with central mass estimates are listed in Table 7, while a histogram of condensation masses is presented in Figure 4(b). To calculate the gas-to-stellar mass ratio, we assume that the central mass within 100 au is dominated by the stellar mass, thus $M_\star \approx M_c \sin^2 i$ (i.e., ignoring the inclination angle correction, see below). Figure 6(a) presents the gas-to-stellar mass ratio vs. radius relation from the DIHCA sample and the intermediate and high-mass points in M. T. Beltrán & W. J. de Wit (2016). Note that there is an overlap between the DIHCA sample and the data compiled by M. T. Beltrán & W. J. de Wit (2016), but their stellar masses are estimated from simulated clusters and based on lower angular resolution observations than DIHCA. The dependence of the central mass on inclination would make

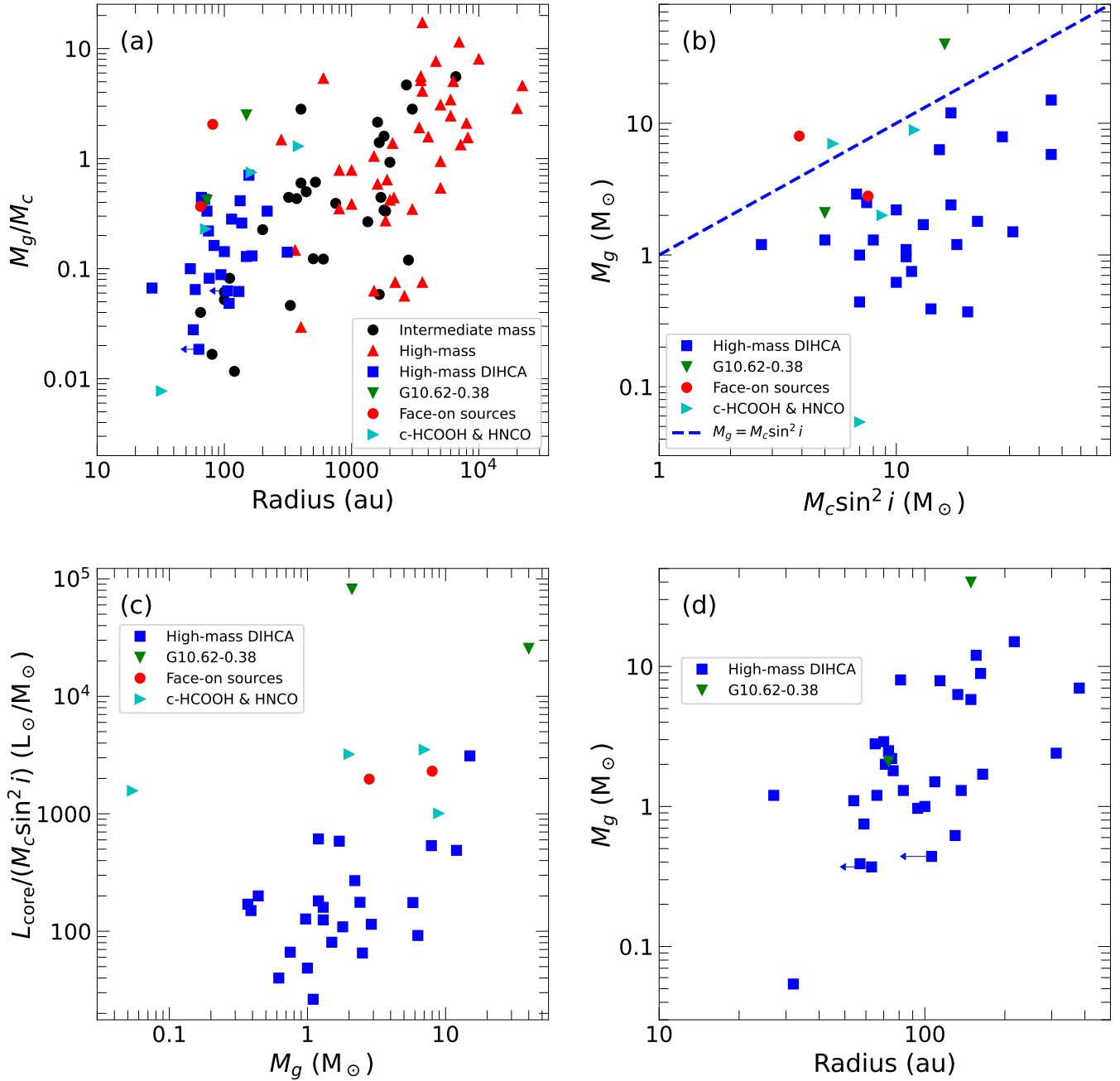


Figure 6. Relations between measured quantities. The blue squares show the results from the DIHCA sample without sources considered as outliers. (a) The M_g/M_\star relation, with $M_\star = M_c \sin^2 i$, as a function of condensation radius. The black circles and red triangles show the results summarized by M. T. Beltrán & W. J. de Wit (2016) for intermediate-mass and high-mass star forming regions, respectively. (b) The gas mass as a function of central source mass. The dashed blue line shows the 1:1 ratio. (c) The evolutionary tracer L_\star/M_\star versus gas mass. Outliers are indicated in red circles, and cyan and green triangles (see details in §4.2). (d) The disk candidate mass as a function of its radius. The green triangles show the outliers in G10.62-0.38, whose 1.3 mm flux density is likely contaminated by free-free emission.

our estimation of M_\star a lower limit. Similarly, the dust opacity is relatively low compared with other opacity laws (e.g., $1\text{ cm}^2\text{ g}^{-1}$ from V. Ossenkopf & T. Henning 1994, $1.9\text{ cm}^2\text{ g}^{-1}$ for proto-planetary disks in T. Birnstiel et al. 2018) and the dust temperature can also be higher since the used value may represent the colder envelope component of the core, hence the estimation of M_g would be an upper limit for the sources corrected for the optical depth. The masses without optical depth correction are slightly underestimated (a few solar masses) compared to those with the correction. However, N. Añez-López et al. (2020) estimated a disk mass of 5 M_\odot for IRAS 18162–2048 ALMAe1 from radiative transfer modeling, which is slightly lower than M_g^{thin} . Thus, the estimated M_g/M_\star would be an upper limit in most cases.

Our results at ~ 230 au spatial resolution are located in the area of the most compact intermediate sources and separated from the previous high-mass results, thus confirming the lack of angular resolution hypothesis. Omitting the H II region source G10.62–0.38, 22 out of 30 condensations (73%) have gas masses that are lower than 5 M_\odot . This is a significant fraction of the sources compared to the 7 out 13 sources below 5 M_\odot in A. Ahmadi et al. (2023, 54%), but in line with the mass of the fragments in Cygnus-X from X. Pan et al. (2025, $< 3\text{ M}_\odot$). On the other hand, the condensations are slightly more compact than the fragments in X. Pan et al. (2025, effective radii > 200 au), with 27 out of 30 with radius smaller than 200 au (90%). Given that many of the condensations have Keplerian-like rotation and that their radii is smaller than our angular resolution, they constitute a good sample of disk candidates. In the more nearby sources with Keplerian power-laws, our observations may be mapping the outer regions of the disk, while power-laws between -0.5 and -1.0 may indicate that the observations are mapping a transition zone. In this transition zone the superposition of the motions of an unresolved Keplerian disk and the rotating and infalling envelope would explain the observed power-law indices.

Figure 6(b) indicates that the distribution of condensation masses is relatively flat compared to that of the central source masses, with only a weak dependency (Figure 5). Hence, massive disks may not necessarily be needed to form the most massive stars. This could be the result of high-accretion rates which can be attained in part from accretion burst due to fragmentation or large scale streamers, or feedback may have already started to destroy the dust thus resulting in smaller gas masses on the sources with H II regions. In addition, we explore whether the condensation masses vary with evolution

by using the evolutionary indicator L_\star/M_\star , where L_\star is the stellar luminosity. For proto-stellar masses higher than about 5 M_\odot , L_\star/M_\star increases as the stellar mass increases, with the rate of increment a function of the accretion rate (H. Zinnecker & H. W. Yorke 2007). Since most sources in Table 5 are the only condensation with line emission associated to its respective core, we assume that the luminosity from the condensation with line emission dominates that of the core, L_{core} , and that $L_\star \approx L_{\text{core}}$. We use the luminosity calculated as part of the ATLASGAL survey (J. S. Urquhart et al. 2018). This luminosity is derived from single-dish observations (from mid-IR to sub-mm), and thus represents the clump luminosity, L_{clump} , containing multiple cores resolved in Paper IV. As an approximation, we scale the luminosity by the 1.3 mm flux density contribution of each core, $S_{1.3\text{ mm}}^{\text{core}}$, in a given clump/field:

$$L_{\text{core}} = \frac{S_{1.3\text{ mm}}^{\text{core}} L_{\text{clump}}}{\Sigma S_{1.3\text{ mm}}^{\text{core}}}, \quad (6)$$

where $\Sigma S_{1.3\text{ mm}}^{\text{core}}$ is the sum of the flux density values of all the cores in a clump/field. Figure 6(c) shows the L_{core}/M_\star ratio as a function of the gas mass. Excluding outliers, we found that there is a weak positive correlation between the evolutionary indicator and the condensation mass (Spearman correlation coefficient of 0.33 and a p-value of 0.11). Given the presence of gas close to the central sources we could assume that they are still in their accretion phase, as confirmed by the evidence of outflows. The gas masses are thus high enough to avoid feedback effects (e.g., radiation, ionization, winds), particularly for those with masses larger than 20 M_\odot (A. L. Rosen 2022). If the gas mass available is independent of evolution, as the weak correlation in Figure 6(c) seems to show, the disk-candidates may be constantly being fed by the larger envelope. In turn, disks can become more massive at any point of the formation process depending on the infall rate and the available gas in the larger scales. Similarly, we do not find a correlation between L_\star/M_\star and the radius of the disk candidates (Spearman correlation coefficient of 0.33, p-value of 0.14), indicating that their size do not depend on the source evolutionary stage. On the other hand, the moderate correlation between the sizes and masses of the disk candidates (Figures 5 and 6(d)) seems to imply that inflows bring gas that can build up massive and large disks. These large disks can be thus transitory as the low frequency of these type of sources in the DIHCA sample shows (cf. histograms in Figure 4). These evidences indicate that anisotropic accretion through, e.g., streamers can play an important role in feeding the disks at a rate sufficient to maintain the high densities needed to overcome

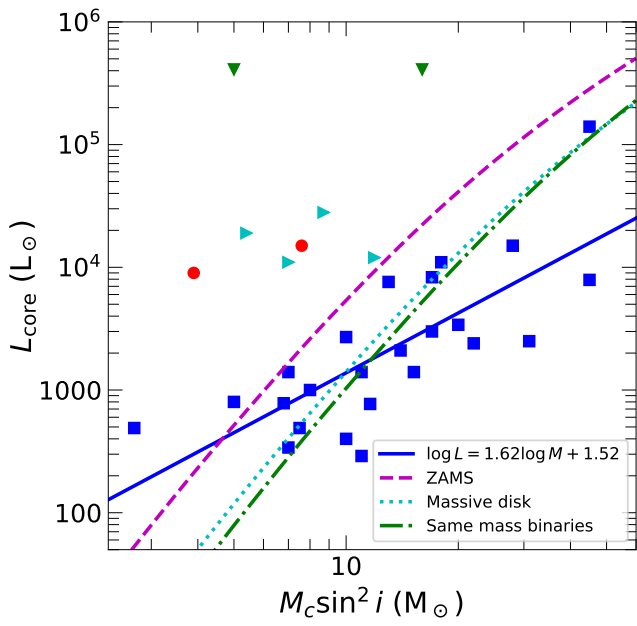


Figure 7. Mass-luminosity relation for the sources in Table 5. The point shapes and colors are the same as in Figure 6(c). The dashed magenta line shows the mass-luminosity relation for main sequence stars from the stellar models of S. Ekström et al. (2012), the blue line show the power law fit to the blue squares, the dotted cyan line shows the relation expected for single stars with massive disks and the dash-dotted green line shows the relation expected for equal-mass binary systems.

the feedback and feed the stars as demonstrated by recent case studies (F. A. Olgun et al. 2025; X. Mai et al. 2025).

We explore whether a relation between the central/stellar masses and the luminosity, similar to that of main-sequence stars, holds at this stage or not. Figure 7 shows that most of the sources have a luminosity lower than the ZAMS luminosity (from S. Ekström et al. 2012) at the estimated dynamical masses. The luminosity at the formation stage is expected to be higher than ZAMS at a given central source mass due to the contribution of the accretion luminosity (e.g., K. E. I. Tanaka et al. 2017). Hence this is strikingly problematic, particularly at the higher central mass end where this trend is present even when the clump luminosity is considered (see Figure C2 in Appendix C). This may suggest that the total dynamical mass is not confined to single stars, but rather distributed in multiple systems or stars surrounded by massive, optically thick disks at smaller scales. As illustrative cases, we plot the expected curves for an equal-mass binary and a single star with a massive disk, which better match the observed mass-luminosity

relation. To derive these relations, we first interpolate the ZAMS curve from S. Ekström et al. (2012) to derive the $L_{\text{ZAMS}}(M_{\star})$ function, then an equal-mass binary system will have a luminosity $L_{\star} = 2L_{\text{zams}}(M_{\star}/2)$ and the luminosity of a single star with a massive disk is $L_{\star} = L_{\text{ZAMS}}(M_{\star}/1.5)$. Given the high fraction of close companions among massive stars (H. Sana et al. 2012), the presence of unresolved proto-stellar companions or compact disks at $< 100\text{--}300\text{ au}$ scales is to be expected. Alternatively, the luminosity may have been underestimated due to source morphology whereby radiation escapes through a different line of sight, hence affecting the emission at the peak of the spectral energy distribution. Excluding outliers, we obtain a Spearman correlation coefficient of 0.77 (p-value of 10^{-5}), indicative of a strong correlation, and we fit a power law of the form $\log L_{\star} = 1.62 \log M_c + 1.52$ (dash-dotted green line in Figure 7).

4.3. Gravitational stability

In order to assess whether the sources can fragment, allowing the formation of binary/multiple systems, or develop substructures like spiral arms, we calculate the Toomre- Q stability parameter. Following A. Ahmadi et al. (e.g., 2023):

$$Q = \frac{c_s \Omega}{\pi G \Sigma} \quad (7)$$

with the speed of sound

$$c_s = \sqrt{\frac{\gamma k_B T}{\mu m_H}} \quad (8)$$

where k_B is the Boltzmann constant and m_H the hydrogen mass. Similar to A. Ahmadi et al. (2023) and X. Pan et al. (2025), we use an adiabatic index $\gamma = 7/5$ and a mean molecular weight $\mu = 2.8$. The angular velocity is

$$\Omega = \sqrt{\frac{G(M_g + M_c \sin^2 i)}{R^3}} \quad (9)$$

and the surface density $\Sigma = M_g/(\pi R^2)$ with R the condensation radius. Figure 4(d) shows a histogram of the Toomre- Q values listed in Table 7. Although the condensations in DIHCA at $\sim 230\text{ au}$ scales differ from the those in the CORE program at 1000 au (H. Beuther et al. 2018; A. Ahmadi et al. 2023), at the smaller scales most sources remain gravitationally unstable (ignoring outliers, 17 out of 22). Sources in the DIHCA sample have Toomre- Q values in the 0.07–12 range with a median of ~ 0.5 . The extreme values seem to be outliers with the lowest one corresponding to G10.62–0.38

ALMAe1, whose gas mass is uncertain, and the highest one corresponding to NGC 6334I ALMAe4, which has the lowest gas mass in the sample like due to it relatively high gas temperature compared with the other sources. Among the stable sources are G335.579–0.272 ALMAe4, which may have a companion, and G336.01–0.82 ALMAe3, which indicates that it may still hold a small stable disk fed by streamers. While G35.03+0.35 A ALMAe1 seems also to be stable, its radius is not well constrained.

4.4. Kinematics tracers

In this work we have used different molecules to trace the kinematics of the hot cores close to the forming stars. As the explored transitions have different upper level energies, they may be tracing different layers of gas. Here we explore what is the effect of the molecular line selection on the resulting source properties of G333.12–0.56 ALMAe1 and G333.46–0.16 ALMAe1. We select these sources because they have kinematics resolved in CH₃OH and CH₃CN, while G333.46–0.16 ALMAe1 also has HNCO (one of the additional molecules used), with the same channel width. The PV maps in Figure 2 show that they have a relatively well fitted Keplerian profile.

Figure 8(a) shows the PV map from CH₃CN $J_K = 12_3 - 11_3$ in G333.12–0.56 ALMAe1 with its power law fit following the same procedure as for CH₃OH $J_{K_a, K_c} = 18_{3,15} - 17_{4,14} A$, $v_t = 0$. The resulting power law index α from a boundless fit is -0.7 ± 0.1 which is higher than the one obtained from CH₃OH ($\alpha = -0.56 \pm 0.06$). Similarly, if the outlier edge points with velocities higher than -48 km s^{-1} are omitted the power law index is $\alpha = -0.61 \pm 0.07$, still consistent within the uncertainties but expected if CH₃CN is tracing in part colder regions associated with a rotating and infalling envelope. On the other hand, the mass within 100 au from the Keplerian fit to the CH₃CN emission is $20 \pm 2 M_\odot$ (with and without outliers), which is roughly $5 M_\odot$ higher than that derived from CH₃OH but still within the uncertainties at the 3σ level.

Figures 8(b) and (c) show a different distribution than that from HNCO for G333.46–0.16 ALMAe1. In general, HNCO emission is more compact than CH₃CN and CH₃OH, even for the sources in NGC 6334I. The PV maps in Figure 2 in the rotation and its orthogonal directions and the power law fit indicate that the HNCO emission is not Keplerian. The first order moment map in Figure 1 seems to indicate that the kinematics traced by HNCO are more complex. On the other hand, CH₃CN and CH₃OH are tracing roughly the same component. Using the velocity extrema, we obtain the same source mass, $16 M_\odot$, within a radius of 750 and

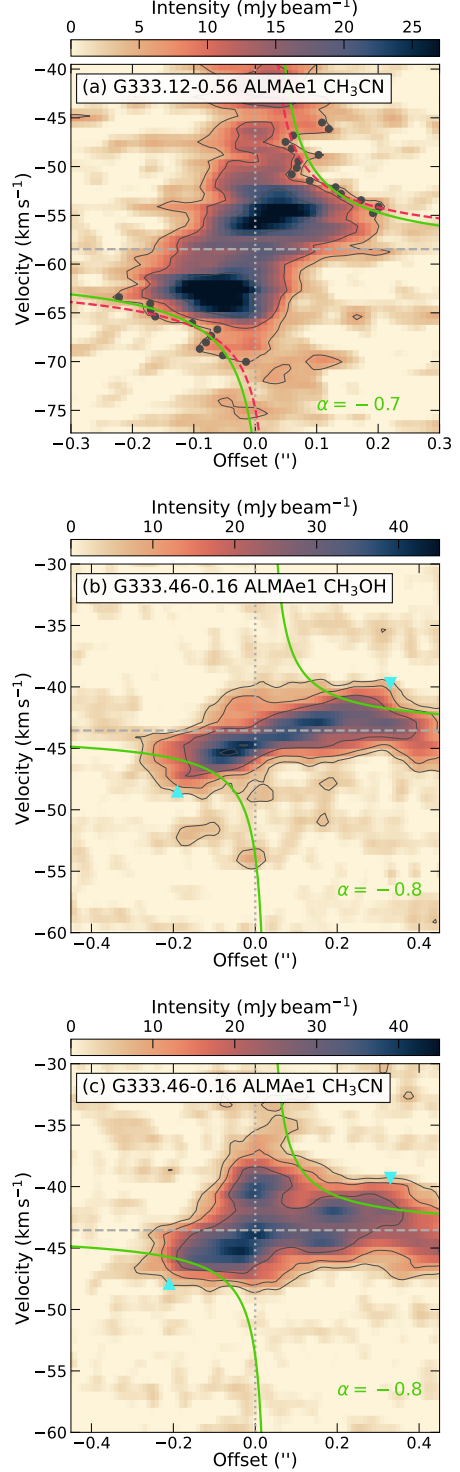


Figure 8. Position-velocity maps from CH₃OH and CH₃CN emission for selected sources along the rotation direction. (a) The cyan circles indicate the edge points, and the continuous gray and dashed red lines show the boundless and Keplerian power law fits to the edge points, respectively. (b) The cyan triangles indicate the position of the velocity extrema determined from the edge points. The gray lines show the boundless model fitted to the HNCO emission in Figure 2. The dotted vertical and dashed horizontal green lines indicate the zero position offset and the systemic velocity in Table 4, respectively.

780 au for CH₃OH and CH₃CN, respectively. Therefore, these two sources show that there is no clear cut between the source properties derived from CH₃OH and CH₃CN. This is also supported by the histogram of power-law indices in Figure 4. Detailed radiative transfer modeling of the emission of these molecules in future studies would provide more accurate physical properties.

Finally, c-HCOOH was used for IRAS 18162–2048 ALMAe1 and a relatively good power law fit was obtained. Although the lack of CH₃OH and CH₃CN precludes a detailed study of what this molecular line emission is tracing, the central mass derived from the fitting is in line to that estimated from the detailed study performed by [M. Fernández-López et al. \(2023\)](#).

Even though CH₃CN and CH₃OH seem to be tracing similar kinematics, this may not be true in general across observations mapping different scales. For instance, [C. J. Law et al. \(2021\)](#) found structured emission of complex organic molecules in G10.62–0.38 at intermediate scales (few hundred to thousand au scales) that trace different kinematics, albeit in one of the more evolved regions in the DIHCA sample. At smaller scales, CH₃OH abundance may decrease close to the central source due to reactions with H₃⁺ ([R. T. Garrod & E. Herbst 2006](#)), making them appear weaker and thus hindering their ability to trace the gas motion of disks. These two issues could be addressed in future works by using principal component analysis in order to determine the best tracers for the same gas components that could be used at different scales (e.g., [Y. Okuda et al. 2021](#)) in addition to chemical models.

4.5. Infall and rotation to form high-mass stars

In this work we have shown that the disk candidates have Keplerian-like rotation, but also exhibit hints of infall. Table 7 summarizes the gas motions in the disk candidates. We propose that high-mass stars form at the center of envelope/disk systems, whereby an unstable envelope channel gas inward from scales orders of magnitude larger than those of the disks. The unstable envelopes can fragment, allowing the formation of companions, and/or develop preferential channels to feed the disks at high infall rates (e.g., [F. A. Olgun et al. 2025](#)). Anisotropic collapse can also be attained or triggered by interaction with other sources in clustered environments (e.g., [X. Lu et al. 2022](#)). The constant streaming of fresh gas allow to maintain a high density in the zone close to the star to avoid feedback effects, like quenching of accretion. Anisotropic collapse can also help to build up some of the larger and massive, albeit short-lived, Keplerian disks observed (e.g., [K. G. Johnston et al. 2020](#)). As the gas joins the disk, the inflows tran-

sition to Keplerian rotation resulting in a region where spectral indices of the power-law PV levels change, and where infall shocks are expected. These shocks can be studied in future works from some of the shock tracers in the DIHCA spectral coverage (e.g., SO, SiO).

5. CONCLUSIONS

We systematically observed 30 fields forming high-mass stars at 1.3 mm with ALMA as part of the DIHCA project. These high-angular resolution observations resolve the kinematics between \sim 230 au scales. We search for molecular line emission mainly from the well-known kinematic tracers CH₃OH and CH₃CN in order to study the circumstellar gas. Of the 30 fields, 49 condensations have line emission over the 5σ detection level to study their kinematics.

Through PV maps, we explore whether the velocity gradients observed in the first moment maps represent rotation. We are able to fit a power law distribution to the PV map edges derived from the contours of the low level emission of 32 sources, that we suggest are disk candidates. With the analysis of the largest, uniformly sample to date of disk-like structures at \sim 230 au scales, we find that power-law indices are mostly distributed in the -0.5 to -1.0 range, with a median of -0.7 . This indicates that the gradient can be explained by Keplerian rotation with some contribution of a rotating and infalling envelope. Future studies performing a detailed modeling of the kinematics would be able to separate the contribution of each component. We provide constraints for another 14 sources while the kinematics cannot be resolved in the remaining 3 sources.

The PV maps also show that the molecular line emission is highly asymmetric on the opposite sides of the central source. We argue that this is the result of anisotropic infall, whereby inflows land at different projected radii along the line of sight and perhaps with different angular momentum vectors. This would result in enhancement of molecular line emission due to density and/or temperature increments. Given that the mass of the disk candidates are relatively independent of the central source masses, these inflows should play an important role in continuously feeding the central region and eventually the star in order to oppose the feedback as the stellar mass increases.

We conclude that the DIHCA observations reveal the regime at which we begin to separate/distinguish disks from envelopes in high-mass hot cores. This results in sources that are more compact and less massive than those derived by early ALMA observations. More sensitive observations will be needed to increase the detection of lines from fainter sources in order to increase the

number statistics and bridge the gap to the low-mass proto-stellar population. At the same time higher angular resolution observations will allow us to determine whether the compact disks are stable and how the inflows feed them.

ACKNOWLEDGMENTS

F.O. and Y.O. acknowledge the support of the NAOJ ALMA Joint Scientific Research Program grant No. 2024-27B. P.S. was partially supported by a Grant-in-Aid for Scientific Research (KAKENHI Number JP23H01221) of JSPS. F.O. and H.-R.V.C. acknowledge the support from the National Science and Technology Council (NSTC) of Taiwan grants NSTC 112-2112-M-007-041 and NSTC 112-2811-M-007-048. Y.O. acknowledges the support by Grant-in-Aids from Ministry of Education, Culture, Sports, Science, and Technologies of Japan (KAKENHI; 21K13954, 25K07367). R.G.M acknowledges support from UNAM-DGAPA-PAPIIT project IN105225. QY-L acknowledges the support by JSPS KAKENHI Grant Number JP23K20035. K.E.I.T. and S.Z. acknowledge support from the NAOJ ALMA Scientific Research Grant Code 2025-29B. K.E.I.T. acknowledges the support by JSPS KAKENHI Grant Number JP 25K07365. K.T. is supported by JSPS KAKENHI grant Nos. 21H01142, 24K17096, and 24H00252. G.G. acknowledges support by the ANID BASAL project FB210003. X.L. acknowledges support from the Strategic Priority Research Program of the Chinese Academy of Sciences (CAS) Grant No.

XDB0800300, the National Key R&D Program of China (No. 2022YFA1603101), State Key Laboratory of Radio Astronomy and Technology (CAS), the National Natural Science Foundation of China (NSFC) through grant Nos. 12273090 and 12322305, the Natural Science Foundation of Shanghai (No. 23ZR1482100), and the CAS “Light of West China” Program No. xbzg-zdsys-202212. This paper makes use of the following ALMA data: ADS/JAO.ALMA#2016.1.01036.S and #2017.1.00237.S. ALMA is a partnership of ESO (representing its member states), NSF (USA) and NINS (Japan), together with NRC (Canada), MOST and ASIAA (Taiwan), and KASI (Republic of Korea), in cooperation with the Republic of Chile. The Joint ALMA Observatory is operated by ESO, AUI/NRAO and NAOJ. Data analysis was in part carried out on the Multi-wavelength Data Analysis System operated by the Astronomy Data Center (ADC), National Astronomical Observatory of Japan. The Scientific color maps vik and lipari ([F. Cramer 2023](#)) are used in this work to prevent visual distortion of the data and exclusion of readers with color vision deficiencies ([F. Cramer et al. 2020](#)).

Facilities: ALMA

Software: Astropy ([Astropy Collaboration et al. 2013, 2018, 2022](#)), CASA ([CASA Team et al. 2022](#)), Scipy ([P. Virtanen et al. 2020](#)), YCLEAN ([Y. Contreras et al. 2018; Y. Contreras 2018; F. Olguin 2025](#)), GoContinuum ([F. Olgun & P. Sanhueza 2020](#)), statcont ([Á. Sánchez-Monge et al. 2018](#))

APPENDIX

A. AUTO-MASKING IMPROVEMENTS

For the cube cleaning, we modified/improved the auto-masking routine YCLEAN ([Y. Contreras et al. 2018; Y. Contreras 2018](#)). The algorithm performs several iterations of `tclean` with an incremental mask calculated from the results of each iterations, and can be divided in three steps: initial (dirty) clean, main cycle, and final clean. From the initial step parameters are calculated from a dirty run of `tclean` (`niter=0`), and include the secondary lobe level from the PSF image (`secondary_lobe`), the rms calculated from image data over a primary beam level of 0.2 using the median average deviation over a sample of channels (`rms`), and residual maximum (`residual_max`). At each iteration of the main cycle the rms and residual maximum are recalculated, and a limit level based on the signal-to-noise ratio (SNR) is calculated as:

$$\text{limit_level_snr} = \text{secondary_lobe_level} \frac{\text{residual_max}}{\text{rms}}. \quad (\text{A1})$$

. The iterations run until one of the following conditions is achieved:

- `limit_level_snr > min_limit_level` where the input parameter `min_limit_level` is set to a default value of 1.5.
- The iteration limit is achieved (default value of 10 iterations).

- The residual maximum increases.
- The corrected residual maximum (see below) is below the threshold of the final iteration (set to 2rms).

For each iteration in the main cycle a mask level and cleaning threshold are calculated. The mask level (`mask_level`) is defined as:

$$\text{mask_level} = (\text{limit_level_snr} + 1.5 \exp(-(|\text{limit_level_snr} - 1.5|)/1.5)) \text{rms}. \quad (\text{A2})$$

For each mask, small clusters of pixels are removed if their areas are smaller than half the beam at a given channel. The threshold is calculated as:

$$\text{threshold} = (0.4 + \arctan(\text{secondary_lobe_level} - 0.2)) \text{residual_max}. \quad (\text{A3})$$

This is an improvement on the determination of the threshold from earlier implementations of YCLEAN, where for higher values of the secondary lobe level the threshold did not decrease with iterations. We implement a corrected `limit_level_snr` and `residual_max` when the new maximum residual value (calculated at the end of the cleaning cycle) is within a tolerance level of the one from the previous iteration in order to keep decreasing the threshold and mask values. The tolerance is set as default as 0.01rms and the corrected values are 0.8^nresidual_max and $0.8^n\text{limit_level_snr}$, where n is the number of times the correction has been applied. Finally, a mask with a 3rms level is produced and a final `tclean` run with a threshold level of 2rms is performed.

B. EDGE PARAMETERS

In order to determine the PV map edges, we use contour levels based on the rms noise of the PV maps (determined from the rms on a line free region). This defines regions over an $n\sigma$ level. We use the largest (or the two largest if the central source is in absorption like in the case of IRAS 18162–2048) contiguous region over the level to extract the edge points as described in §3.2. Since some sources have line forests and/or wider lines that can produce a larger region joining two or more lines, we introduce limits in velocity in the edge extraction. Similarly, some sources may be connected to emission of a common envelope gas, thus we also introduce limits in offset for these cases. Table 8 lists the rms (σ), levels over the rms used (n), and limits in velocity and offset used in the edge calculations.

To assess the effects of the levels selected, we run the same edge extraction and fitting procedures for levels between $3 - \max(5, n)$ with n in Table 8 and in steps of 1. In general, and as expected, higher contours over the noise level result in lower masses. Larger variations in mass are obtained for the brightest sources (e.g., G11.92–0.61 ALMAe1, IRAS 18089–1732 ALMAe1) with variations of roughly $8 M_{\odot}$ for levels between 3 to $7 - 8\sigma$, but in general changes are around $2 - 3 M_{\odot}$ for levels between 3 and 5σ (with the exception of sources with erratic results). Higher levels should produce masses that are more accurate, but since the PV maps are not smooth worse fits may be obtained for higher levels. This seems to have a larger effect on the values of the power law index, α , which do not have a clear trend. Nevertheless variations of α values are generally within ~ 0.3 .

C. SUPPLEMENTARY FIGURES

Figure C1 shows the peak spectra of the 32 disk candidates, calculated as the average in a circle of radius $0''.05$ centered in the source positions in Table 4. Figure C2 shows the mass-luminosity relation with the luminosity of each source equal to that of the clump.

REFERENCES

Añez-López, N., Osorio, M., Busquet, G., et al. 2020, *ApJ*, 888, 41, doi: [10.3847/1538-4357/ab5dbc](https://doi.org/10.3847/1538-4357/ab5dbc)

Ahmadi, A., Beuther, H., Bosco, F., et al. 2023, *A&A*, 677, A171, doi: [10.1051/0004-6361/202245580](https://doi.org/10.1051/0004-6361/202245580)

Aso, Y., Ohashi, N., Saigo, K., et al. 2015, *ApJ*, 812, 27, doi: [10.1088/0004-637X/812/1/27](https://doi.org/10.1088/0004-637X/812/1/27)

Astropy Collaboration, Robitaille, T. P., Tollerud, E. J., et al. 2013, *A&A*, 558, A33, doi: [10.1051/0004-6361/201322068](https://doi.org/10.1051/0004-6361/201322068)

Astropy Collaboration, Price-Whelan, A. M., Sipőcz, B. M., et al. 2018, *AJ*, 156, 123, doi: [10.3847/1538-3881/aabc4f](https://doi.org/10.3847/1538-3881/aabc4f)

Astropy Collaboration, Price-Whelan, A. M., Lim, P. L., et al. 2022, *ApJ*, 935, 167, doi: [10.3847/1538-4357/ac7c74](https://doi.org/10.3847/1538-4357/ac7c74)

Table 8. PV map edge parameters

Source	ALMAe	σ	Level	Velocity range		Offset range	
				Source	(mJy beam $^{-1}$)	(km s $^{-1}$)	(arcsec)
G10.62–0.38	1	1.6	4	–10	8	–0.5	0.5
	3	1.6	6	–0.5	0.5
G11.1–0.12	1	1.3	3
G11.92–0.61	1	1.1	8	20	50
	4	1.1	4
	6	1.1	3
G14.22–0.50 S	3	1.3	3
G29.96–0.02	1	1.4	5	85	110
G333.12–0.56	1	1.8	3
	8	1.7	3
G333.23–0.06	6	1.1	5
	17	1.3	3	–0.38	0.1
G333.46–0.16	1 ^a	1.7	4	–50	–35
	1 ^b	1.9	3
	2	1.7	3
G335.579–0.272	1	1.4	4
	4	1.4	3
G335.78+0.17	1	1.6	6
	2	1.8	3
G336.01–0.82	3	1.7	4
G34.43+0.24 MM1	2	1.3	6	–0.5	0.5
G343.12–0.06	1	1.1	6
G35.03+0.35 A	1	1.9	5
G35.13–0.74	1	2.5	5
	2	2.5	6
	7	2.5	5
G35.20–0.74 N	1	2.5	6
	2	2.5	3	–0.35	0.5
G5.89–0.37	1	1.8	6
IRAS 16562–3959	1	1.4	6
	4	1.4	6
IRAS 18089–1732	1	1.6	7	20	46	–0.7	0.7
	2	1.6	4
IRAS 18162–2048	1	1.2	5	–0.4	0.4
IRAS 18182–1433	1	1.4	5
	2	1.4	3
	5	1.4	4
	11	1.4	6
NGC 6334I	1	1.5	5
	3	1.5	3
	4	1.5	4
NGC 6334I(N)	1	1.5	3
	2	1.5	3
	8	1.7	3
	9	1.7	3
	14	1.7	3
W33A	1	1.3	3	–0.5	0.5
	4	1.3	6

^a For HNCO.^b For CH₃OH and CH₃CN.

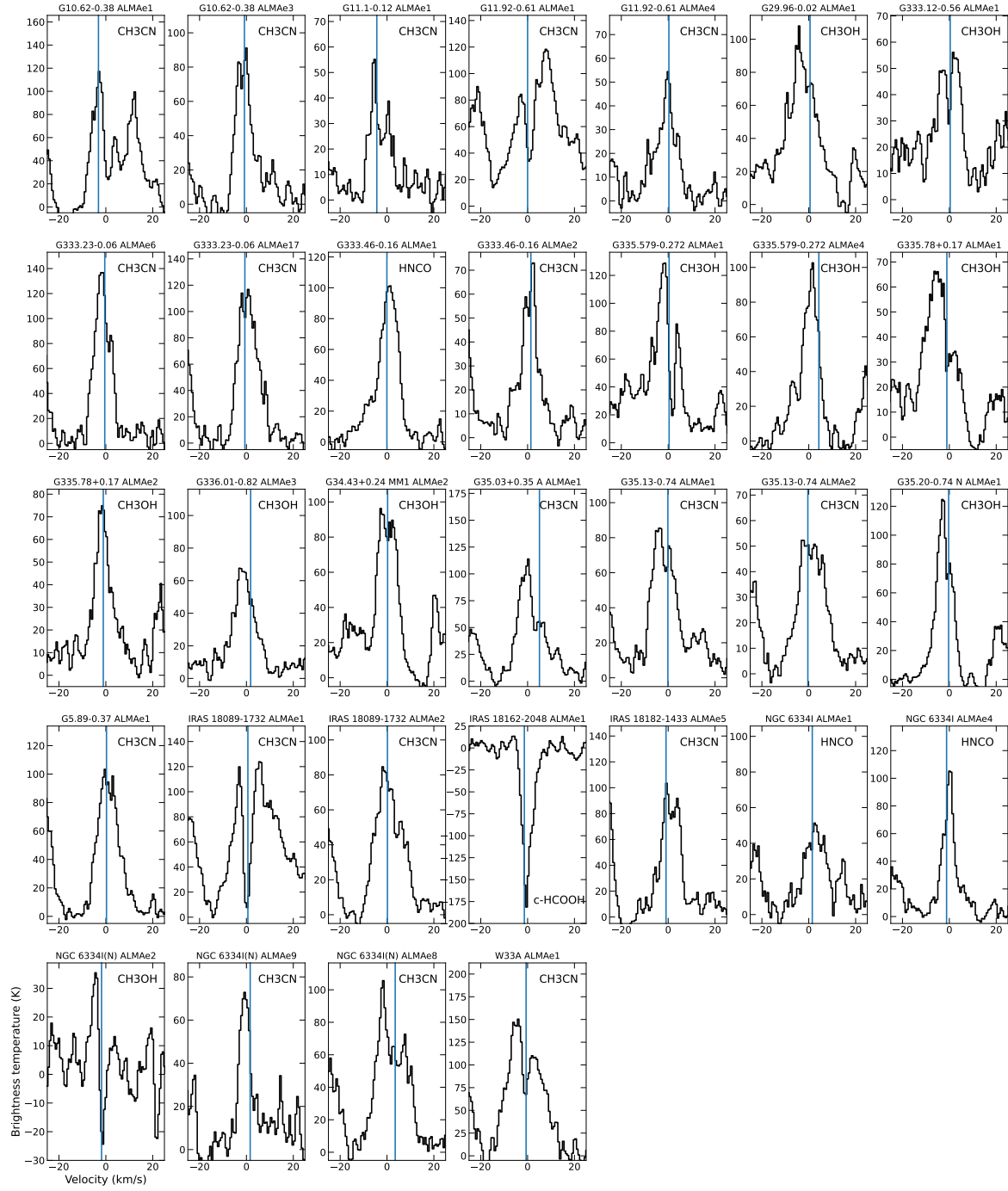


Figure C1. Peak spectra calculated as the average with a circle of radius $0''.05$ centered in the source continuum position. The blue vertical line shows the velocity offset between the v_{LSR} in Table 4 (set to zero velocity) and the systemic velocity obtained through the power law fit to the PV map edges in Table 5.

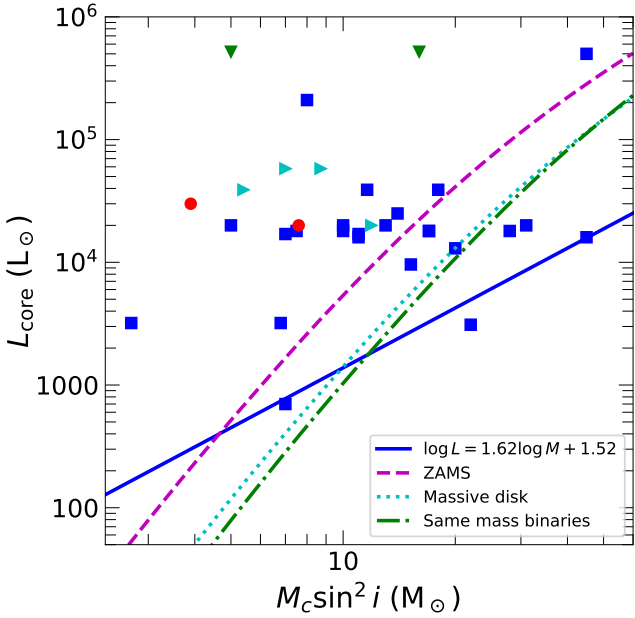


Figure C2. Central sources mass-luminosity relation with the luminosity set to that of the clump. The line and point types are the same as in Figure 6(d).

Avison, A., Fuller, G. A., Peretto, N., et al. 2021, A&A, 645, A142, doi: [10.1051/0004-6361/201936043](https://doi.org/10.1051/0004-6361/201936043)

Bate, M. R. 2018, MNRAS, 475, 5618, doi: [10.1093/mnras/sty169](https://doi.org/10.1093/mnras/sty169)

Beltrán, M. T., & de Wit, W. J. 2016, A&A Rv, 24, 6, doi: [10.1007/s00159-015-0089-z](https://doi.org/10.1007/s00159-015-0089-z)

Beltrán, M. T., Sánchez-Monge, Á., Cesaroni, R., et al. 2014, A&A, 571, A52, doi: [10.1051/0004-6361/201424031](https://doi.org/10.1051/0004-6361/201424031)

Beuther, H., Kuiper, R., & Tafalla, M. 2025a, ARA&A, 63, 1, doi: [10.1146/annurev-astro-013125-122023](https://doi.org/10.1146/annurev-astro-013125-122023)

Beuther, H., Olgun, F. A., Sanhueza, P., Cunningham, N., & Ginsburg, A. 2025b, A&A, 695, A51, doi: [10.1051/0004-6361/202452754](https://doi.org/10.1051/0004-6361/202452754)

Beuther, H., Walsh, A. J., Johnston, K. G., et al. 2017, A&A, 603, A10, doi: [10.1051/0004-6361/201630126](https://doi.org/10.1051/0004-6361/201630126)

Beuther, H., Hunter, T. R., Zhang, Q., et al. 2004, ApJL, 616, L23, doi: [10.1086/383570](https://doi.org/10.1086/383570)

Beuther, H., Mottram, J. C., Ahmadi, A., et al. 2018, A&A, 617, A100, doi: [10.1051/0004-6361/201833021](https://doi.org/10.1051/0004-6361/201833021)

Beuther, H., Ahmadi, A., Mottram, J. C., et al. 2019, A&A, 621, A122, doi: [10.1051/0004-6361/201834064](https://doi.org/10.1051/0004-6361/201834064)

Birnstiel, T., Dullemond, C. P., Zhu, Z., et al. 2018, ApJL, 869, L45, doi: [10.3847/2041-8213/aaf743](https://doi.org/10.3847/2041-8213/aaf743)

Carrasco-González, C., Galván-Madrid, R., Anglada, G., et al. 2012, ApJL, 752, L29, doi: [10.1088/2041-8205/752/2/L29](https://doi.org/10.1088/2041-8205/752/2/L29)

CASA Team, Bean, B., Bhatnagar, S., et al. 2022, PASP, 134, 114501, doi: [10.1088/1538-3873/ac9642](https://doi.org/10.1088/1538-3873/ac9642)

Cesaroni, R., Galli, D., Neri, R., & Walmsley, C. M. 2014, A&A, 566, A73, doi: [10.1051/0004-6361/201323065](https://doi.org/10.1051/0004-6361/201323065)

Cesaroni, R., Sánchez-Monge, Á., Beltrán, M. T., et al. 2017, A&A, 602, A59, doi: [10.1051/0004-6361/201630184](https://doi.org/10.1051/0004-6361/201630184)

Chen, H.-R. V., Keto, E., Zhang, Q., et al. 2016, ApJ, 823, 125, doi: [10.3847/0004-637X/823/2/125](https://doi.org/10.3847/0004-637X/823/2/125)

Commerçon, B., González, M., Mignon-Risse, R., Hennebelle, P., & Vaytet, N. 2022, A&A, 658, A52, doi: [10.1051/0004-6361/202037479](https://doi.org/10.1051/0004-6361/202037479)

Contreras, Y. 2018, Automatic Line Clean, 1.0 Zenodo, doi: [10.5281/zenodo.1216881](https://doi.org/10.5281/zenodo.1216881)

Contreras, Y., Sanhueza, P., Jackson, J. M., et al. 2018, ApJ, 861, 14, doi: [10.3847/1538-4357/aac2ec](https://doi.org/10.3847/1538-4357/aac2ec)

Cortés, P. C., Sanhueza, P., Houde, M., et al. 2021, ApJ, 923, 204, doi: [10.3847/1538-4357/ac28a1](https://doi.org/10.3847/1538-4357/ac28a1)

Cortés, P. C., Girart, J. M., Sanhueza, P., et al. 2024, ApJ, 972, 115, doi: [10.3847/1538-4357/ad59a7](https://doi.org/10.3847/1538-4357/ad59a7)

Crameri, F. 2023, Scientific colour maps, 8.0.1 Zenodo, doi: [10.5281/zenodo.8409685](https://doi.org/10.5281/zenodo.8409685)

Crameri, F., Shephard, G. E., & Heron, P. J. 2020, Nature Communications, 11, 5444, doi: [10.1038/s41467-020-19160-7](https://doi.org/10.1038/s41467-020-19160-7)

Cunningham, A. J., Klein, R. I., Krumholz, M. R., & McKee, C. F. 2011, ApJ, 740, 107, doi: [10.1088/0004-637X/740/2/107](https://doi.org/10.1088/0004-637X/740/2/107)

Cyganowski, C. J., Brogan, C. L., Hunter, T. R., Churchwell, E., & Zhang, Q. 2011, ApJ, 729, 124, doi: [10.1088/0004-637X/729/2/124](https://doi.org/10.1088/0004-637X/729/2/124)

Cyganowski, C. J., Brogan, C. L., Hunter, T. R., et al. 2017, MNRAS, 468, 3694, doi: [10.1093/mnras/stx043](https://doi.org/10.1093/mnras/stx043)

Cyganowski, C. J., Illee, J. D., Brogan, C. L., et al. 2022, ApJL, 931, L31, doi: [10.3847/2041-8213/ac69ca](https://doi.org/10.3847/2041-8213/ac69ca)

Dominik, C., Min, M., & Tazaki, R. 2021, OpTool: Command-line driven tool for creating complex dust opacities,, Astrophysics Source Code Library, record ascl:2104.010

Dullemond, C. P., Küffmeier, M., Goicovic, F., et al. 2019, A&A, 628, A20, doi: [10.1051/0004-6361/201832632](https://doi.org/10.1051/0004-6361/201832632)

Ekström, S., Georgy, C., Eggenberger, P., et al. 2012, A&A, 537, A146, doi: [10.1051/0004-6361/201117751](https://doi.org/10.1051/0004-6361/201117751)

Fernández-López, M., Girart, J. M., López-Vázquez, J. A., et al. 2023, ApJ, 956, 82, doi: [10.3847/1538-4357/ace786](https://doi.org/10.3847/1538-4357/ace786)

Fernández-López, M., Sanhueza, P., Zapata, L. A., et al. 2021, ApJ, 913, 29, doi: [10.3847/1538-4357/abf2b6](https://doi.org/10.3847/1538-4357/abf2b6)

Garrod, R. T., & Herbst, E. 2006, A&A, 457, 927, doi: [10.1051/0004-6361:20065560](https://doi.org/10.1051/0004-6361:20065560)

Ginsburg, A., McGuire, B. A., Sanhueza, P., et al. 2023, ApJ, 942, 66, doi: [10.3847/1538-4357/ac9f4a](https://doi.org/10.3847/1538-4357/ac9f4a)

Goddi, C., Ginsburg, A., Maud, L. T., Zhang, Q., & Zapata, L. A. 2020, *ApJ*, 905, 25, doi: [10.3847/1538-4357/abc88e](https://doi.org/10.3847/1538-4357/abc88e)

Guzmán, A. E., Sanhueza, P., Zapata, L., Garay, G., & Rodríguez, L. F. 2020, *ApJ*, 904, 77, doi: [10.3847/1538-4357/abbe09](https://doi.org/10.3847/1538-4357/abbe09)

Ilee, J. D., Cyganowski, C. J., Brogan, C. L., et al. 2018, *ApJL*, 869, L24, doi: [10.3847/2041-8213/aaeffc](https://doi.org/10.3847/2041-8213/aaeffc)

Ishihara, K., Sanhueza, P., Nakamura, F., et al. 2024, *ApJ*, 974, 95, doi: [10.3847/1538-4357/ad630f](https://doi.org/10.3847/1538-4357/ad630f)

Izquierdo, A. F., Galván-Madrid, R., Maud, L. T., et al. 2018, *MNRAS*, 478, 2505, doi: [10.1093/mnras/sty1096](https://doi.org/10.1093/mnras/sty1096)

Johnston, K. G., Robitaille, T. P., Beuther, H., et al. 2015, *ApJL*, 813, L19, doi: [10.1088/2041-8205/813/1/L19](https://doi.org/10.1088/2041-8205/813/1/L19)

Johnston, K. G., Hoare, M. G., Beuther, H., et al. 2020, *A&A*, 634, L11, doi: [10.1051/0004-6361/201937154](https://doi.org/10.1051/0004-6361/201937154)

Krumholz, M. R., Klein, R. I., & McKee, C. F. 2007a, *ApJ*, 656, 959, doi: [10.1086/510664](https://doi.org/10.1086/510664)

Krumholz, M. R., Klein, R. I., & McKee, C. F. 2007b, *ApJ*, 665, 478, doi: [10.1086/519305](https://doi.org/10.1086/519305)

Krumholz, M. R., Klein, R. I., McKee, C. F., Offner, S. R., & Cunningham, A. J. 2009, *Science*, 323, 754, doi: [10.1126/science.1165857](https://doi.org/10.1126/science.1165857)

Kuiper, R., & Hosokawa, T. 2018, *A&A*, 616, A101, doi: [10.1051/0004-6361/201832638](https://doi.org/10.1051/0004-6361/201832638)

Law, C. J., Zhang, Q., Öberg, K. I., et al. 2021, *ApJ*, 909, 214, doi: [10.3847/1538-4357/abdeb8](https://doi.org/10.3847/1538-4357/abdeb8)

Li, S., Sanhueza, P., Beuther, H., et al. 2024, *Nature Astronomy*, 8, 472, doi: [10.1038/s41550-023-02181-9](https://doi.org/10.1038/s41550-023-02181-9)

Li, S., Beuther, H., Oliva, A., et al. 2025, *Nature Astronomy*, 9, 1833, doi: [10.1038/s41550-025-02682-9](https://doi.org/10.1038/s41550-025-02682-9)

Lu, X., Li, G.-X., Zhang, Q., & Lin, Y. 2022, *Nature Astronomy*, 6, 837, doi: [10.1038/s41550-022-01681-4](https://doi.org/10.1038/s41550-022-01681-4)

Luo, Q., Sanhueza, P., Offner, S. S. R., et al. 2026, Digging into the Interior of Hot Cores with ALMA. VI. The Formation of Low-mass Multiple Systems in High-mass Cluster-forming Regions, <https://arxiv.org/abs/2601.08904>

Mai, X., Liu, T., Liu, X., et al. 2025, *Science Advances*, 11, eady6953, doi: [10.1126/sciadv.ady6953](https://doi.org/10.1126/sciadv.ady6953)

Maud, L. T., Hoare, M. G., Galván-Madrid, R., et al. 2017, *MNRAS*, 467, L120, doi: [10.1093/mnrasl/slx010](https://doi.org/10.1093/mnrasl/slx010)

Maud, L. T., Cesaroni, R., Kumar, M. S. N., et al. 2019, *A&A*, 627, L6, doi: [10.1051/0004-6361/201935633](https://doi.org/10.1051/0004-6361/201935633)

Meyer, D. M. A., Vorobyov, E. I., Kuiper, R., & Kley, W. 2017, *MNRAS*, 464, L90, doi: [10.1093/mnrasl/slw187](https://doi.org/10.1093/mnrasl/slw187)

Mohan, N., & Rafferty, D. 2015, PyBDSF: Python Blob Detection and Source Finder, *Astrophysics Source Code Library*, record ascl:1502.007 <http://ascl.net/1502.007>

Momose, M., Ohashi, N., Kawabe, R., Nakano, T., & Hayashi, M. 1998, *ApJ*, 504, 314, doi: [10.1086/306061](https://doi.org/10.1086/306061)

Mori, S., Aikawa, Y., Oya, Y., Yamamoto, S., & Sakai, N. 2024, *ApJ*, 961, 31, doi: [10.3847/1538-4357/ad0634](https://doi.org/10.3847/1538-4357/ad0634)

Okuda, Y., Oya, Y., Abe, S., et al. 2021, *ApJ*, 923, 168, doi: [10.3847/1538-4357/ac2c6c](https://doi.org/10.3847/1538-4357/ac2c6c)

Olguin, F. 2025, Improved and updated YCLEAN, v2.3.0 Zenodo, doi: [10.5281/zenodo.17197133](https://doi.org/10.5281/zenodo.17197133)

Olguin, F., & Sanhueza, P. 2020, GoContinuum: continuum finding tool, v2.0.0 Zenodo, doi: [10.5281/zenodo.4302846](https://doi.org/10.5281/zenodo.4302846)

Olguin, F. A., Sanhueza, P., Ginsburg, A., et al. 2022, *ApJ*, 929, 68, doi: [10.3847/1538-4357/ac5bd8](https://doi.org/10.3847/1538-4357/ac5bd8)

Olguin, F. A., Sanhueza, P., Guzmán, A. E., et al. 2021, *ApJ*, 909, 199, doi: [10.3847/1538-4357/abde3f](https://doi.org/10.3847/1538-4357/abde3f)

Olguin, F. A., Sanhueza, P., Chen, H.-R. V., et al. 2023, *ApJL*, 959, L31, doi: [10.3847/2041-8213/ad1100](https://doi.org/10.3847/2041-8213/ad1100)

Olguin, F. A., Sanhueza, P., Ginsburg, A., et al. 2025, *Science Advances*, 11, eadw4512, doi: [10.1126/sciadv.adw4512](https://doi.org/10.1126/sciadv.adw4512)

Ossenkopf, V., & Henning, T. 1994, *A&A*, 291, 943

Oya, Y., Kibukawa, H., Miyake, S., & Yamamoto, S. 2022, *PASP*, 134, 094301, doi: [10.1088/1538-3873/ac8839](https://doi.org/10.1088/1538-3873/ac8839)

Oya, Y., & Yamamoto, S. 2020, *ApJ*, 904, 185, doi: [10.3847/1538-4357/abbe14](https://doi.org/10.3847/1538-4357/abbe14)

Oya, Y., Sakai, N., Sakai, T., et al. 2014, *ApJ*, 795, 152, doi: [10.1088/0004-637X/795/2/152](https://doi.org/10.1088/0004-637X/795/2/152)

Pan, X., Qiu, K., & Zhang, Q. 2025, *A&A*, 696, A195, doi: [10.1051/0004-6361/202452944](https://doi.org/10.1051/0004-6361/202452944)

Pouteau, Y., Motte, F., Nony, T., et al. 2022, *A&A*, 664, A26, doi: [10.1051/0004-6361/202142951](https://doi.org/10.1051/0004-6361/202142951)

Rosen, A. L. 2022, *ApJ*, 941, 202, doi: [10.3847/1538-4357/ac9f3d](https://doi.org/10.3847/1538-4357/ac9f3d)

Saha, P., Sanhueza, P., Padovani, M., et al. 2024, *ApJL*, 972, L6, doi: [10.3847/2041-8213/ad660c](https://doi.org/10.3847/2041-8213/ad660c)

Sai, J., Ohashi, N., Saigo, K., et al. 2020, *ApJ*, 893, 51, doi: [10.3847/1538-4357/ab8065](https://doi.org/10.3847/1538-4357/ab8065)

Sakai, T., Shiomura, N., Sanhueza, P., et al. 2025, *ApJ*, 983, 37, doi: [10.3847/1538-4357/abda5a](https://doi.org/10.3847/1538-4357/abda5a)

Sana, H., de Mink, S. E., de Koter, A., et al. 2012, *Science*, 337, 444, doi: [10.1126/science.1223344](https://doi.org/10.1126/science.1223344)

Sanchez-Monge, A. 2019, in ALMA2019: Science Results and Cross-Facility Synergies, 122, doi: [10.5281/zenodo.3585445](https://doi.org/10.5281/zenodo.3585445)

Sánchez-Monge, Á., Schilke, P., Ginsburg, A., Cesaroni, R., & Schmiedeke, A. 2018, *A&A*, 609, A101, doi: [10.1051/0004-6361/201730425](https://doi.org/10.1051/0004-6361/201730425)

Sánchez-Monge, Á., Cesaroni, R., Beltrán, M. T., et al. 2013, *A&A*, 552, L10, doi: [10.1051/0004-6361/201321134](https://doi.org/10.1051/0004-6361/201321134)

Sánchez-Monge, Á., Beltrán, M. T., Cesaroni, R., et al. 2014, *A&A*, 569, A11, doi: [10.1051/0004-6361/201424032](https://doi.org/10.1051/0004-6361/201424032)

Sanhueza, P., Girart, J. M., Padovani, M., et al. 2021, ApJL, 915, L10, doi: [10.3847/2041-8213/ac081c](https://doi.org/10.3847/2041-8213/ac081c)

Sanhueza, P., Liu, J., Morii, K., et al. 2025, ApJ, 980, 87, doi: [10.3847/1538-4357/ad9d40](https://doi.org/10.3847/1538-4357/ad9d40)

Seifried, D., Banerjee, R., Pudritz, R. E., & Klessen, R. S. 2015, MNRAS, 446, 2776, doi: [10.1093/mnras/stu2282](https://doi.org/10.1093/mnras/stu2282)

Seifried, D., Sánchez-Monge, Á., Walch, S., & Banerjee, R. 2016, MNRAS, 459, 1892, doi: [10.1093/mnras/stw785](https://doi.org/10.1093/mnras/stw785)

Tanaka, K. E. I., Tan, J. C., & Zhang, Y. 2017, ApJ, 835, 32, doi: [10.3847/1538-4357/835/1/32](https://doi.org/10.3847/1538-4357/835/1/32)

Tanaka, K. E. I., Zhang, Y., Hirota, T., et al. 2020, ApJL, 900, L2, doi: [10.3847/2041-8213/abadfc](https://doi.org/10.3847/2041-8213/abadfc)

Taniguchi, K., Sanhueza, P., Olguin, F. A., et al. 2023, ApJ, 950, 57, doi: [10.3847/1538-4357/acca1d](https://doi.org/10.3847/1538-4357/acca1d)

Urquhart, J. S., König, C., Giannetti, A., et al. 2018, MNRAS, 473, 1059, doi: [10.1093/mnras/stx2258](https://doi.org/10.1093/mnras/stx2258)

Virtanen, P., Gommers, R., Oliphant, T. E., et al. 2020, Nature Methods, 17, 261, doi: [10.1038/s41592-019-0686-2](https://doi.org/10.1038/s41592-019-0686-2)

Yamamoto, R., Tanaka, K. E. I., & Okuzumi, S. 2025, ApJ, 990, 59, doi: [10.3847/1538-4357/adf49c](https://doi.org/10.3847/1538-4357/adf49c)

Yano, Y., Nakamura, F., & Kinoshita, S. W. 2024, ApJ, 964, 119, doi: [10.3847/1538-4357/ad2a54](https://doi.org/10.3847/1538-4357/ad2a54)

Yorke, H. W., & Bodenheimer, P. 1999, ApJ, 525, 330, doi: [10.1086/307867](https://doi.org/10.1086/307867)

Zapata, L. A., Garay, G., Palau, A., et al. 2019, ApJ, 872, 176, doi: [10.3847/1538-4357/aafedf](https://doi.org/10.3847/1538-4357/aafedf)

Zapata, L. A., Ho, P. T. P., Fernández-López, M., et al. 2020, ApJL, 902, L47, doi: [10.3847/2041-8213/abbd3f](https://doi.org/10.3847/2041-8213/abbd3f)

Zapata, L. A., Fernández-López, M., Sanhueza, P., et al. 2024, ApJ, 974, 257, doi: [10.3847/1538-4357/ad701d](https://doi.org/10.3847/1538-4357/ad701d)

Zhang, S., Cyganowski, C. J., Henshaw, J. D., et al. 2024, MNRAS, 533, 1075, doi: [10.1093/mnras/stae1844](https://doi.org/10.1093/mnras/stae1844)

Zhang, Y., Tan, J. C., Sakai, N., et al. 2019, ApJ, 873, 73, doi: [10.3847/1538-4357/ab0553](https://doi.org/10.3847/1538-4357/ab0553)

Zhang, Y., Tanaka, K. E. I., Tan, J. C., et al. 2022, ApJ, 936, 68, doi: [10.3847/1538-4357/ac847f](https://doi.org/10.3847/1538-4357/ac847f)

Zinnecker, H., & Yorke, H. W. 2007, ARA&A, 45, 481, doi: [10.1146/annurev.astro.44.051905.092549](https://doi.org/10.1146/annurev.astro.44.051905.092549)